UNIVERSITY of CRETE

Department of Materials Science and Technology

Development and Study of Solution Processed Hybrid Perovskite Solar Cells (PeSCs)

Temur Maksudov

Master Thesis

HERAKLION 2018

Supervisors:

Prof. E. Kymakis & Prof. G. Kioseoglou

This work was realized in the Laboratory of “Nanomaterials & Organic Electronics (NANO) Group” headed by Prof. Emmanuel Kymakis, at the Department of Electrical Engineering, part of the School of Engineering of TEI of Crete under the guidance of Dr. George Kakavelakis.

Contents

List of Abbreviations

- AM Air Mass
- AFM Atomic Force Microscope
- a-Si amorphous Silicon
- CB Conduction Band
- DMF Dimethylformamide
- DMSO Dimethylsulfoxide
- DSSC Dye Sensitized Solar Cell
- Eg Energy band gap
- EIA Energy Information Administration
- EQE External Quantum Efficiency
- ETL Electron Transport Layer
- F4-TCNQ (2,3,5,6-Tetrafluoro-2,5-cyclohexadiene-1,4-diylidene) dimalononitrile
- FF Fill Factor
- FTO Fluorine doped Tin Oxide
- GDP Gross Domestic Product
- HTL Hole Transport Layer
- IQE Internal Quantum Efficiency
- I_{sc} & J_{sc} Short Circuit Current & Short Circuit Current density
- ITO Indium Tin Oxide
- MAI Methylammonium iodide
- $MAPbI_3$ Methylamonium lead iodide
- MoS_2 Molybdenum Disulfide
- OPV Organic Photovoltaic
- $PbCl_2$ Lead Chloride
- PbI_2 Lead Iodide
- $PCBM_{60}$ [6,6]-phenyl-C61-butyric acid methyl ester
- PCE Power Conversion Efficiency
- PEDOT:PSS Poly(3,4-ethylenedioxythiophene) polystyrene sulfonate
- PeSC Perovskite Solar Cell
- PHJ Planar heterojunction structure
- PV Photo Voltaic
- PL Photoluminescence
- PFN Poly [(9,9-bis(3'-(N,N-dimethylamino)propyl)-2,7-fluorene)-alt-2,7-(9,9–dioctylfluorene)]
- rGO reduced graphene oxide

- SEM Scanning Electron Microscope
- TCO Transparent Conductive Oxide
- UV-Vis Ultraviolet-Visible spectroscopy
- VB Valence Band
- V_{oc} Open Circuit Voltage
- XRD X-Ray Diffraction

Abstract

Developing countries and emerging markets demands for environmental friendly renewable energy sources continuously increases. Renewable energy technology and especially photovoltaics is an alternative solution that gains ground year after year to replace the established carbon consuming energy production methods. One of the latest and of high potential photovoltaics' generation technology is the so-called perovskite solar cells (PeSCs). A PeSC consists of a laminated structure, which is being developed layer by layer using facile deposition methods onto rigid and flexible substrates. Organic-inorganic hybrid perovskite is a material with the crystal structure AMX_3, where A is the organic part, M is the metal and X stands for a halide ion. Since 2009 when the first application of organohalide lead perovskite as the light harvester in solar cells was reported [1], tremendous attention has been devoted to these new types of perovskite-based solid-state solar cells and remarkable power conversion efficiency of over 22% has been achieved up to date[2]. With respect to its hybrid nature, the material is endowed with high carrier mobility and absorption coefficient, relatively long diffusion lengths and low temperature processing, that renders it ideal for optoelectronic applications. During the implementation of this thesis, the mixed halide perovskite ($MAPbI_{3-x}Cl_x$) and methylammonium lead triiodide perovskite ($MAPbI_3$) were synthesized and applied as light harvesting material in planar inverted PSCs. In our case the hybrid perovskite semiconductor selected, was deposited using the spin coating deposition technique on top of glass/ITO/(PEDOT:PSS or PTAA) substrate and after that the deposition of an electron transport material followed. To complete the device, thermal evaporation was used to form the silver counter electrode. A variety of factors (annealing temperature of the perovskite, morphology, different HTLs and additives to the hole and electron transport layers) that play a critical role towards the achievement of high and stable power conversion efficiencies (PCEs) were studied and applied.

Acknowledgments

I would like to thank Prof. Emmanuel Kymakis who has given me the opportunity to join his group and work on such an interesting project, for his encouraging attitude and support as well as Prof. George Kioseoglou from Material Science and Technology Department for his supervision. I would also thank Dr. George Kakavelakis for his guidance, support and encouragement that helped me understanding the phenomena I was working with. Finally, I want to thank all group members, Prof. Konstantinos Petridis, Dr. Minas Stylianakis, Dr. Dimitris Konios, Mr. Myron Krassas (PhD), Mr. George Viskadouros (PhD), Pavlos Tzourmpakis (MSc), Valina Foustanaki (MSc) Anna Orfanoudaki (MSc) and Apostolos Panagiotopoulos (Undergraduate) for their assistance and kindness.

1. Introduction

As the world population risen, it is expected the global energy demands to increase as well. It is estimated that by 2050 the world population will exceed the nine billion people (**Figure 1-1)**[3]. Increasing energy demands and concerns about global warming trigger the exploration and development of environmental friendly, inexpensive and renewable energy sources.

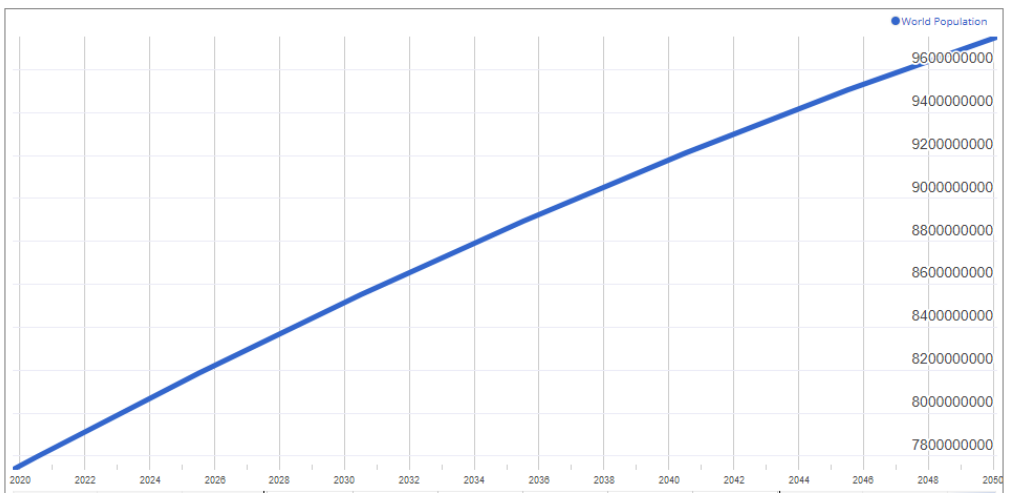

Figure 1-1 Estimated population growth by 2040 [3]

The U.S. Energy Information Administration (EIA) [4] in the recently released International Energy Outlook 2017 (IEO2017) projects refers that:

- With world gross domestic product (GDP) rising by 3.3 percent per year, world energy use will grow by 36 percent between 2015 and 2040. Most of the increase is attributed to China and India, countries in which strong economic growth drives increasing demand for energy.
- Renewable energy and nuclear power are the world's fastest-growing energy sources, each increasing by 2,5 percent per year; however, fossil fuels continue to supply almost 80 percent of world energy use through 2040.
- Given current policies and regulations, worldwide energy-related carbon dioxide emissions are projected to increase 46 percent by 2040, reaching 45 billion metric tons in 2040.

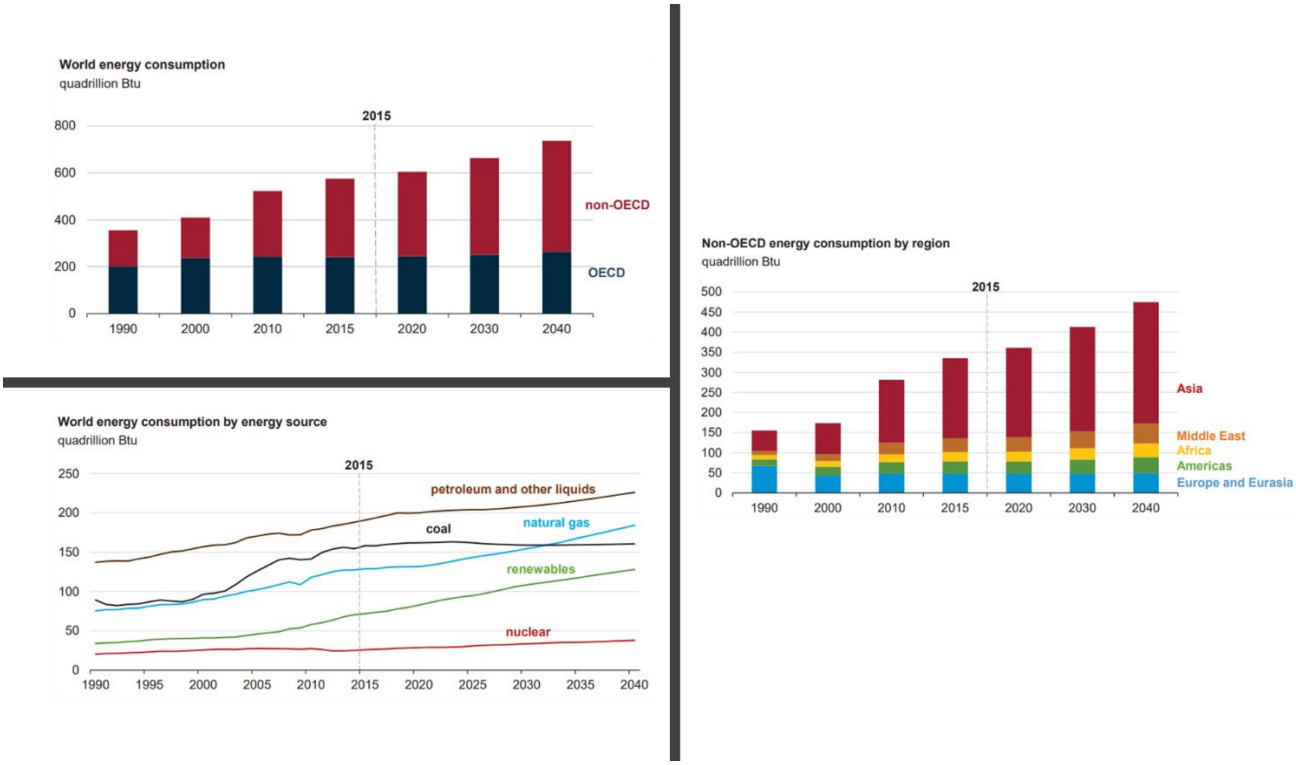

Figure 1-2. World energy consumption data [4]. Organization for Economic Co-operation and Development (OECD) i.e. developed countries, non-OECD i.e. emerging markets. 1 quadrillion Btu = 2.93x1011 KWh.

Taking into consideration the EIA's perspectives and the data illustrated into **Figure 1-2**, the demand for renewable energy sources is growing every day. The most accessible, clean and abundant source is the sun. A years' worth of sunlight contains 1.5× 1018 kWh of energy (**Figure 1-3** Solar radiation spectrum). By comparison, the known reserves of oil, coal, and gas are 1,75 ×1015 kWh, 1,4 ×1015kWh, and 5:5 ×1015 kWh, respectively [2]. Thus, a years' worth of sunlight provides more than a hundred times the energy of the worlds' entire known fossil fuel reserves. Harnessing solar power would yield a never-ending energy supply. In other words, it takes the sun one hour and 25 minutes to send us the amount of energy we currently consume in a year. The difficulty has always been converting solar energy in an efficient and cost-effective way. Photovoltaic cells are the most promising avenue, directly converting the photons to electricity (**Figure 1-4**). For photovoltaic energy to become competitive with fossil fuels and capture a significant share of the electricity market, it is necessary to reduce the total cost of solar energy. This can be achieved by either reducing the cost of photovoltaic cells or by increasing their power conversion efficiency.

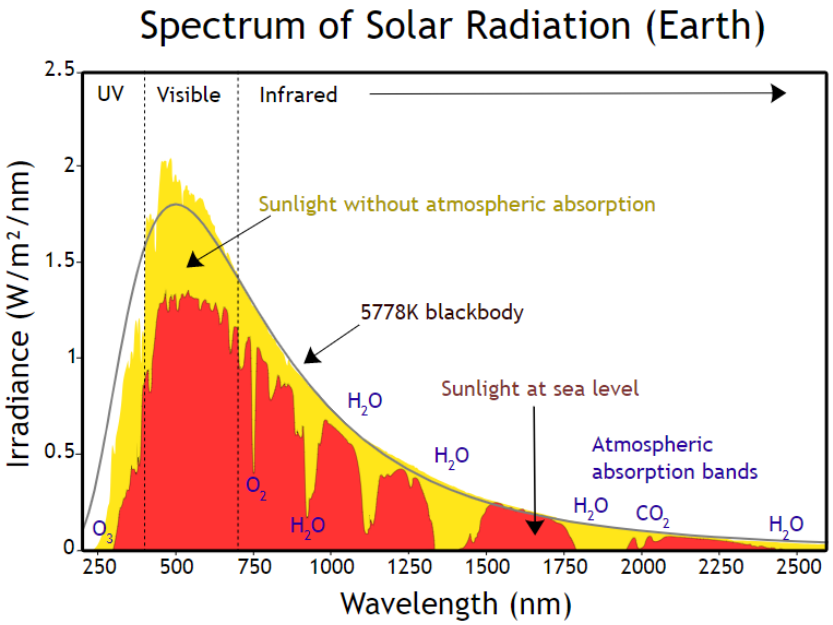

Figure 1-3. Solar radiation spectrum [5].

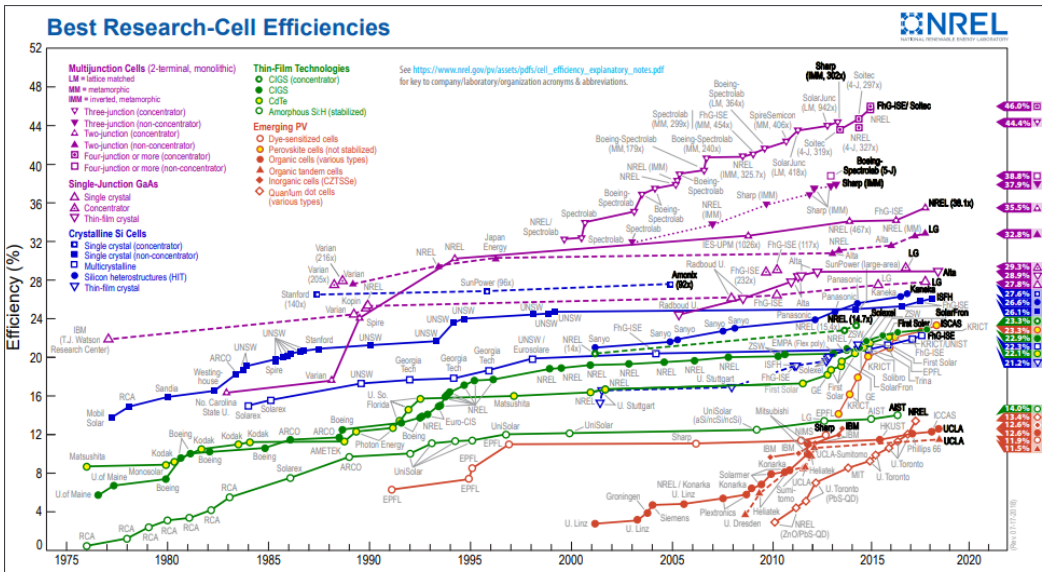

Figure 1-4. Road map for the best research cell efficiencies (National Renewable Energy Laboratory-NREL)[6].

From **Figure 1-4** [4] one can state that, the first-generation silicon PVs have reach 25% in yield, the second-generation thin film PVs are at about 20% and the third-generation multi-junction PVs have exceeded the astonishing 40% in power conversion efficiency. Furthermore, in **Figure 1-5**, the evolution of perovskite solar cells' (PeSC) efficiency is shown with a record efficiency of 23,3% up to date. An exponential increase of PCE for the PeSC is observed in the last 5 years. These efficiencies are high enough to justify the increased interest for the PeSCs and to intrigue for further research activity.

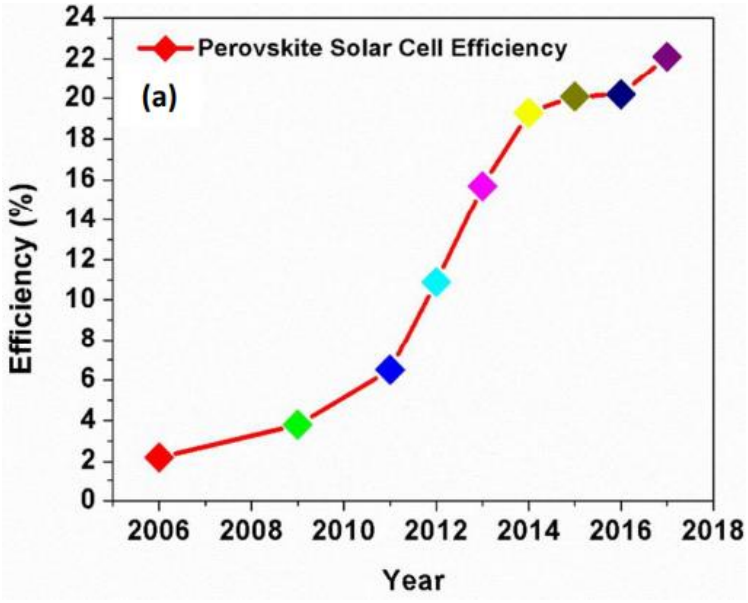

Figure 1-5. The evolution of PeSC efficiency over the past few years. [7]

2. Theoretical Background

2.1 History of perovskite

Perovskite is a name of the mineral calcium titanate ($CaTiO_3$), but it also lends its name for an extended family of crystals with the same crystal structure as calcium titanate. The mineral was first discovered in 1839 by a German geologist in the Ural Mountains in Russia and named after a Russian geologist Lev Perovski. Perovskite is consisted of two different anionic ions and three cationic ions of the same kind. One of the positive ions has a charge of 2+ and the other a charge of 1+, while the negative ion type has a charge of 1-. This transfers to the general formula of ABX_3 (**Figure 2-1**)[8]. This formula is of course only the simplest form and perovskite structures with more complicated formulas exist, for example $YBa_2Cu_3O_{7-x}$ which is a high temperature processed superconductor. Perovskites of different constitution exhibit a plethora of different physical and chemical properties. Since their discovery and the characterization of their crystal structure, perovskites have been widely studied. Moreover, their tunable attributes have been exploited on many fields of science. For example, some of the applications of perovskites are listed below[9] .

Property	Value	Oxide material	References
Mobility	$\mu = 22\,000\ cm^2 \cdot (V \cdot s)^{-1}$ (2 K)	$SrTiO_3$	Tufte and Chapman[11]
Metal–insulator transition	$\Delta R/R_{T_{low}} > 10^{13}$	EuO	Petrich *et al.*[12]
Superconductivity	$T_c = 135$ K	$HgBa_2Ca_2Cu_3O_{8+x}$	Schilling *et al.*[13]
Ferroelectricity	$P_s = 105\ \mu C/cm^2$	$PbZr_{0.2}Ti_{0.8}O_3$	Vrejoiu *et al.*[14]
	$P_s = 100\ \mu C/cm^2$	$BiFeO_3$	Wang *et al.*,[15] Li *et al.*[16] Das *et al.*,[17] Dho *et al.*[18]
Piezoelectricity	$d_{33} = 2500$ pC/N	$PbZn_{1/3}Nb_{2/3}O_3$–$PbTiO_3$	Park *et al.*[19]
Ferromagnetism	$M_s = 6.9\ \mu_B$/Eu	EuO	Matthias *et al.*[20]
Colossal magnetoresistance	$\Delta R/R_H > 10^{11}$ (5 T)	$Pr_{0.7}Sr_{0.04}Ca_{0.26}MnO_{3-\delta}$	Maignan *et al.*[21]
Magnetostriction	$\lambda_{100} = -590 \times 10^{-6}$	$Co_{0.8}Fe_{2.2}O_4$	Bozorth *et al.*[22]
Faraday effect	$\nu = 4 \times 10^{5\circ} \cdot (T \cdot cm)^{-1}$	EuO	Ahn and Shafer[23]
Spin polarization	$P > 98\%$	CrO_2	Soulen *et al.*,[24] Anguelouch *et al.*[25]
Ferromagnetic and ferroelectric simultaneously	$T_C = 105$ K	$BiMnO_3$	Hill and Rabe,[29] Moreira dos Santos *et al.*,[28] Sharan *et al.*,[30] Baettig *et al.*[31]
	$T_C = 250$ K	$LuFe_2O_4$, $FeTiO_3$	Ikeda *et al.*, Fennie[27]

Table 1. Properties and applications of Perovskite mixed metal oxides.

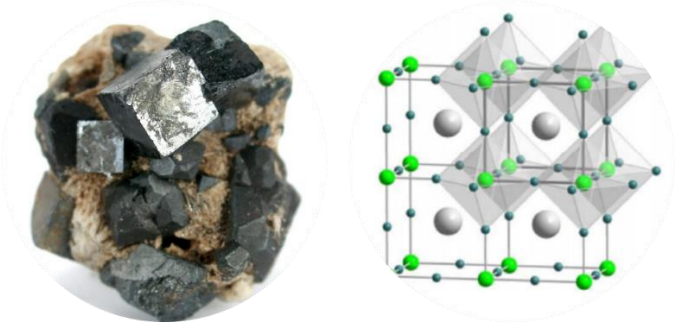

Figure 2-1 A perovskite mineral (left) and the basic perovskite structure ABX_3 (right) [10]

2.2 Hybrid Perovskite based solar cells

Hybrid perovskite combines the advantages of the inorganic and organic materials (**Figure2-2**). It is the same chemical formula ABX_3, but with different ions, A is an organic cation, B is a metal cation and X is a halide anion[10]. Perovskites were first used in photovoltaics by Miyasaka et al in 2009[1]. They made photocells with a liquid phase electrolyte based on mesoporous TiO_2 photocathodes sensitized with $CH_3NH_3PbX_3$ (X=I, Br). They achieved an average PCE of 3.8%, which in comparison with other fields at the time was not very impressive. In terms of structure such a system suffers from fast degradation due to the dissolution of perovskite absorber into the organic electrolyte. Three years later in 2012 Grätzel et al used methylammonium lead triiodide perovskite ($MAPbI_3$) as a light harvester in combination with the solid hole conductor on mesoporous TiO_2 reporting a PCE of 9,7% [11]. This solid-state cell managed to spark new interest in the field of perovskite photovoltaics.

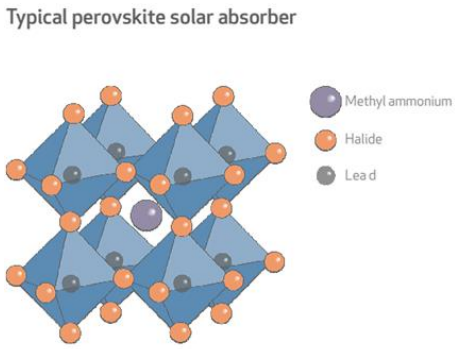

Figure 2-2 Hybrid perovskite [12]

2.3 Device Architectures

2.3.1 Mesoporous structure

A common device configuration for $CH_3NH_3PbI_3$ based solar cells consists of an n-type mesoporous layer infiltrated with the perovskite (**Figure 2-3**). The solar cell fabrication process commences with the deposition of a compact TiO_2 hole-blocking layer on top of the fluorine doped tin oxide (FTO) substrate. On top of the compact layer, a mesoporous layer of n-type TiO_2 is formed afterwards. The perovskite films are then deposited on top of the n-type mesoporous layer. This is followed by the deposition of a hole transporting material (HTM) such as spiro-OMeTAD and finally a metal electrode is thermally evaporated on top of the HTM, to complete the device[13].

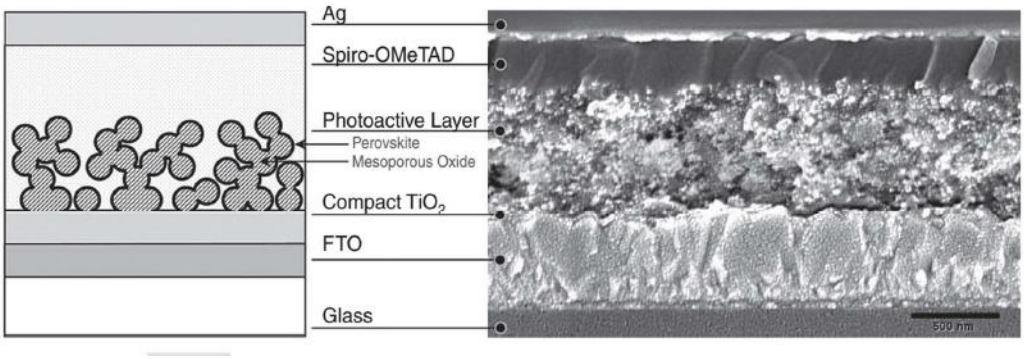

Figure 2-3 (Left) The schematic diagram and (Right) cross-section SEM of the mesoporous structured perovskite solar cell device [13].

2.3.2 Planar heterojunction structure (PHJ)

In a planar junction perovskite solar cell, a several hundred nanometer thick absorber layer is sandwiched between the two transport layer materials (the ETL and HTL) without the use of the mesoporous scaffold (**Figure 2-4**). As the hybrid perovskite exhibits ambipolar carrier transport and long carrier lifetimes, solar cells with planar configurations can deliver efficiency values of over 15%. This architecture offers the advantages of a simplified device configuration and facile fabrication. Planar structures are most commonly illuminated from the n-type side, resulting in the normal structure (glass/TCO (Transparent Conductive Oxide)/ETL/perovskite/HTL/metal), or p-type side, resulting in the inverted structure (glass/TCO/HTL/perovskite/ETL/metal) which functions in a superstrate configuration. All above mentioned indicate the possibility of this planar configuration to be a highly efficient architecture. In fact, a PHJ structure can not only simplify the device fabrication process but also avoid the pore filling problem in the mesostuctured device, which always leads to a large deviation of device performance[13].

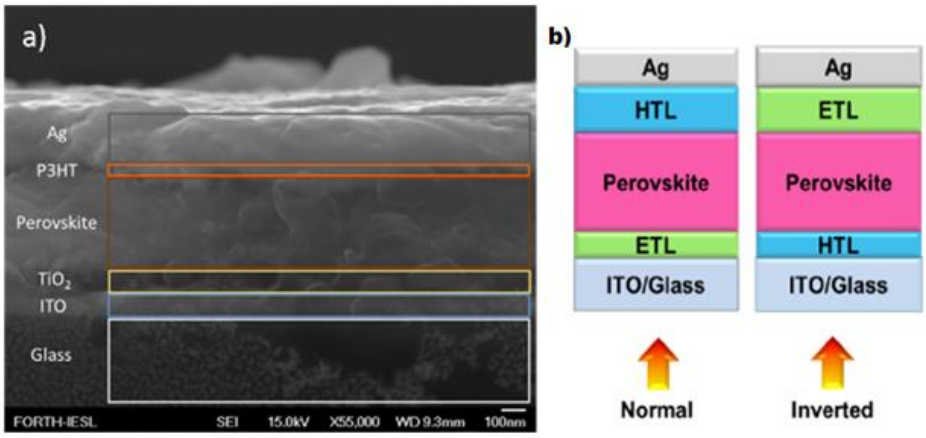

Figure 2-4 (a) Cross section SEM image of normal structure glass/ITO/TiO_2/Perovskite/P3HT/Ag device architecture. The perovskite layer with homogeneous and flat boundaries can be distinguished clearly. (b) The schematic diagram of normal and inverted device architecture[14].

2.4 Operation Mechanism

The operation of perovskite solar cells relies on electron-selective and hole-selective layers that "sandwich" the perovskite layer. The device can also be called a p-i-n junction. In an ideal p-n diode the expression for the current as a function of voltage can be described by the Ideal Diode Law as

$$I = I_0(e^{\frac{qV}{kT}} - 1)$$

where:

I = the net current flowing through the diode

I_0 = "dark saturation current", the diode leakage current density in the absence of light

V = applied voltage across the terminals of the diode

q = absolute value of electron charge

k = Boltzmann's constant

T = absolute temperature (K).

For non-ideal diodes, the expression becomes:

$$I = I_0(e^{\frac{qV}{nkT}} - 1)$$

where n = ideality factor, a number between 1 and 2 typically increases as the current decreases.

The IV curve of a solar cell is the superposition of the IV curve of the solar cell diode in the dark with the light-generated current. The light has the effect of shifting the IV curve down into the fourth quadrant where power can be extracted from the diode (**Figure 2-5**). Illuminating a cell adds to the normal "dark" currents in the diode so that the diode law becomes[15]:

$$I = I_0\left[e^{\frac{qV}{nkT}} - 1\right] - I_L$$

where I_L = light generated current.

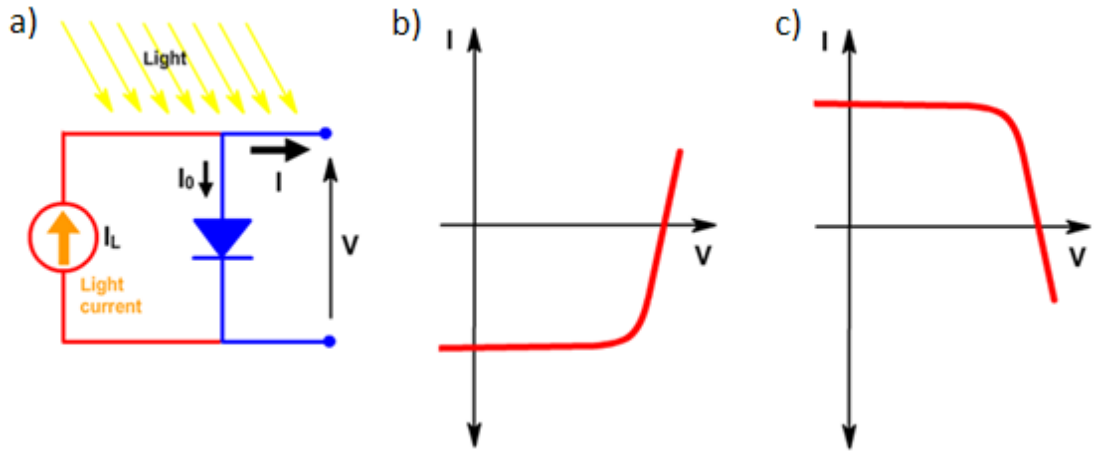

Figure 2-5 a) Diode circuit under illumination. b) When light shines on the cell, the IV curve shifts as the cell begins to generate power. c) Since the cell is generating power, the convention is to invent the current axis [15].

When a photoactive material is illuminated, it can absorb photons with specific energy. This results in an excited state of electrons. The electrons are excited to the CB (conduction band) leaving behind positive holes in the VB (valence band). The valence band is consisted of occupied electron orbitals states when the material is in equilibrium. The conduction band on the other hand is the band of electron orbitals that electrons can occupy when excited from the valence band. The excitation to the CB allows the electrons, after the application of a potential difference, to be able to drift along the atomic lattice. Electrons can move from the valence band to conduction band through absorbing photons of energy equally or a little bit higher that the difference in energy between the maximum point of the VB and the minimum point of the CB (excitation). The energy between these bands is called the energy band gap (Eg). The size of the energy band gap determines whether the material in question is a metal, a semiconductor or an insulator [16] (**Figure 2-6**).

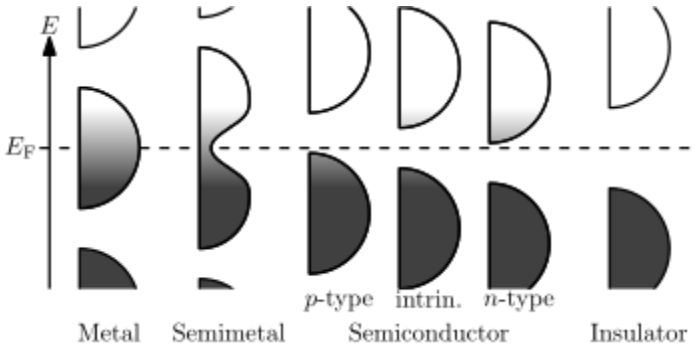

Figure 2-6 The characteristic difference in band gaps for various materials[16].

Once electrons and holes are photo-generated in the perovskite absorber, they are separated at the carrier-selective layers-contacts as each of them blocks one type of carrier and lets the other one to transmit through the respective charge transport layer. An electron-selective layer transports electrons and blocks holes as such, it is called the electron-transport layer (ETL), or hole-blocking layer. Likewise, a hole-transport layer (HTL) transports holes and blocks electrons (**Figure 2-7**). This happens due to the favorable alignment of energy levels of ETL and HTL with the CB and VB of perovskite. Electrons travel to the anode and holes travel to the cathode generating a current and a potential difference, which can be harnessed into electricity. Commonly used anode, like in this work is indium tin oxide (ITO) and the cathode is a metal like silver, aluminum or gold. To reduce carrier recombination at the interfaces, which is detrimental to the open circuit voltage (V_{OC}), the ETL and HTL should be compact and not being heavily doped. So far, both organic and inorganic materials have been identified that are suitable for charge transport layers which are used for producing efficient perovskite solar cells[17] (**Figure 2-8**).

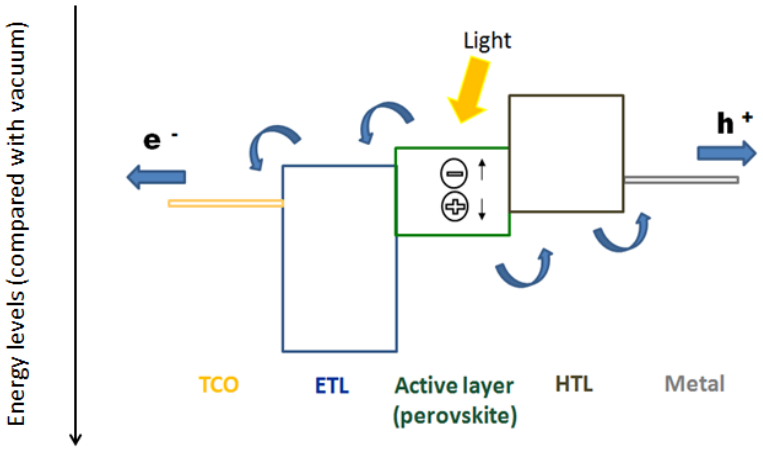

Figure 2-7 The generation and separation of carriers and by HTM and ETL

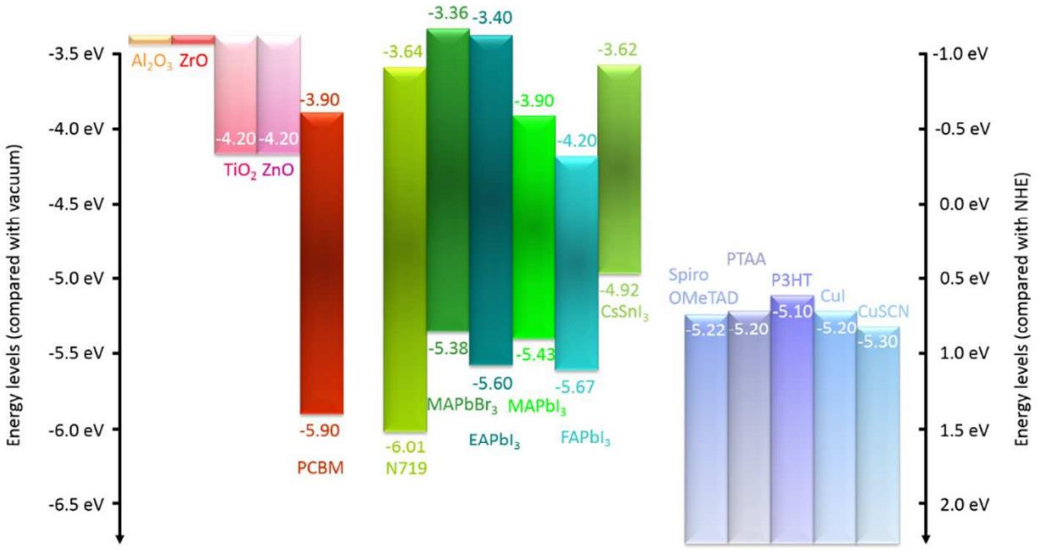

Figure 2-8 Energy levels for different materials acting as electron transport layers (ETL) (left), absorbers (middle) and hole transport layers (HTL) (right) in Perovskite solar cells [17].

Upon illumination, the electron and hole energy levels (called quasi-Fermi levels and denoted EF_n and EF_p, respectively) in the perovskite layer split, driving electrons into the ETL and holes into the HTL (**Figure 2-9**). When this happens, the electron energy levels in the ETL ($E'F_n$) will rise up to an energy position close to the conduction band minimum (CBM), or lowest unoccupied molecular orbital, of the ETL. Similarly, the hole energy level in the HTL ($E'F_p$) will drop to an energy position close to the valence band maximum (VBM), or highest occupied molecular orbital, of the HTL. The difference between $E'F_n$ and $E'F_p$ determines the V_{OC} of the cell as it going to be described in characterization paragraph[18].

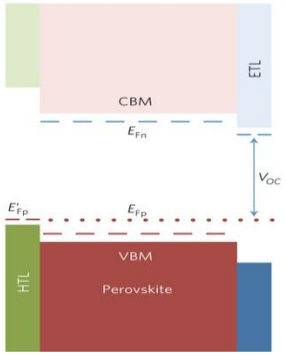

Figure 2-9 General mechanism [17].

2.5 Deposition Methods

One of the key attractions of perovskites is the apparent simplicity of their preparation; however, often a simple procedure belies complex chemistry and dynamics that provide the material its unique morphology and properties. As discussed below, the formation of $CH_3NH_3PbI_3$ in the presence of chloride anions (termed perhaps misleadingly $CH_3NH_3PbI_{3-x}Cl_x$) is an example of such a case. Lead-halide perovskites have been produced primarily by two methods: precipitation from solution and deposition from the vapor phase. Additionally, two-step processes in both solution and vapor phases have been explored. In these reactions, the lead halide is prepared first and then exposed to the methylammonium halide to yield the perovskite (**Figure 2-10**)[19].

2.5.1 One step precursor deposition

In one step precursor deposition method all the precursors of the perovskite are dissolved in a common solvent in the same solution. This is the most widely used method to prepare perovskites due to its simplicity. Solvents used include dimethylformamide (DMF), dimethylsulfoxide (DMSO), and γ-butyrolactone. A sufficiently high amount of perovskite precursors like $PbCl_2$ and Methylammonium iodide (MAI) are dissolved in a solvent and the resulting solution is spin coated onto a suitable substrate. After the deposition the substrate is annealed to finalize the perovskite formation process. Afterwards, hole transporter material is deposited over the active layer. Finally, an electrode is deposited usually via thermal evaporation to complete the device [20].

2.5.2 Sequential deposition method

In the sequential deposition method, the lead halide or a mixture of lead halides are dissolved in a solvent like DMF or γ-butyrolactone (GBL). This solution should be strong enough to ensure good coverage of the substrate in the following spin coating phase. After the substrates have been spin coated they are annealed to evaporate the residual solvent. A solution containing the second precursor is prepared in a solvent that does not interact or dissolve the lead halide prior deposited. After annealing, substrates are dipped in the solution to allow the perovskite formation to take place. Normally, no annealing is required to finish the perovskite formation as the process is almost instantaneous. After the desired dipping time has passed, the slides are removed and annealed again to remove any residual solvent. Once the solvent has evaporated, additional layers are added to the until the whole device to be constructed. This method gives better control over the perovskite morphology than the one step precursor deposition method. Thus, high PCE values can be achieved since the film morphology is one of the key factors affecting perovskite solar cell performance[21].

2.5.3 Dual-source vapor deposition

In this method the perovskite precursors are vaporized, and the substrate is placed so that the both vapors interact with this substrate and form a highly uniform film on it. Once the perovskite film is formed, additional layers of electron or hole transporting materials may be added just like with the other methods described above. This method is not as low cost as the other two described so far, but the uniformity of the films produced might just make up for it. The uniformity of the film makes for increased cell efficiency[20].

2.5.4 Vapor assisted solutions process

This method is a combination of the sequential deposition method and the dual source vapor deposition. The lead halide is spin coated on the substrate just like in sequential deposition method and then methylammonium iodide or another similar molecule is vaporized on it to form the perovskite[20].

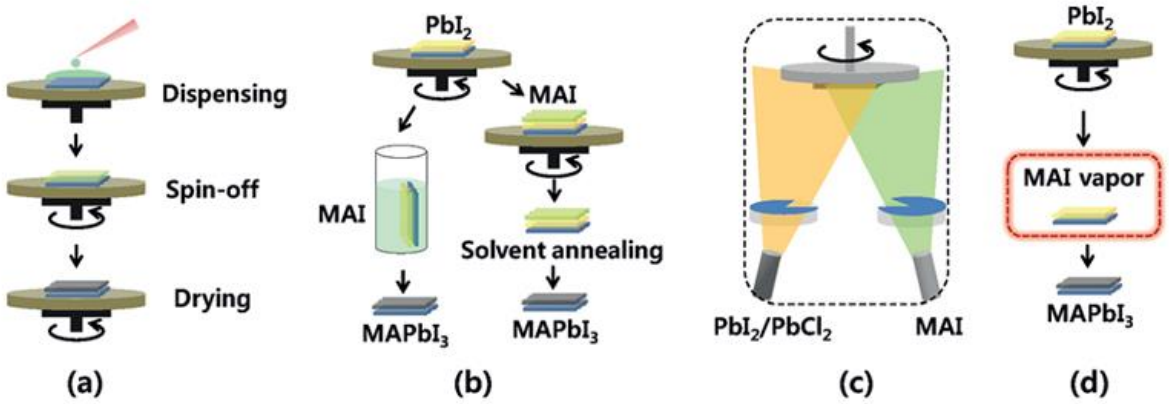

Figure 2-10 Representative deposition methods for perovskite thin film. (a) One-step spin-coating method; (b) sequential deposition method; (c) dual-source vapor deposition; and (d) vapor-assisted solution process[20]

2.6 Role of Cl in the deposition of $CH_3NH_3PbI_3$

The first perovskite solar cells were produced from $CH_3NH_3PbI_3$ precursor solution, and it was later discovered that introduced chloride ions (Cl^-) can modify the crystallization process to improve their photovoltaic performance[22]. Subsequent studies confirmed the superior properties of $CH_3NH_3PbI_{3-x}Cl$ like, its optical absorption is stronger near the band gap[23] and it yields nearly equal electron and hole diffusion lengths of ~1 μm,[24] as compared with the ~100–300 nm measured for typical $CH_3NH_3PbI_3$[25]. This feature allows thicker $CH_3NH_3PbI_{3-x}Cl_x$ layers to fabricate planar heterojunction solar cells compared to thinner $CH_3NH_3PbI_3$ layers. However, it is found that the incorporation of chloride ions does not change the crystalline structures as well as the band structures. Here, it should be noted that the $CH_3NH_3PbI_{3-x}Cl_x$ precursor solution is typically prepared by blending CH_3NH_3I and $PbCl_2$ with a molar ratio of 3:1. Only a small amount of chloride ions (<5%) can remain in the solution-processed thin film[22]. It is further found

that no chloride ions can be detected in the perovskite crystals. As a result, deeper efforts are demanded to explore the effect of the chloride ions in perovskite solar cells.

2.7 Tolerance factor

The formation of perovskite phase is not so trivial. For example, a careful selection of precursors must be done to achieve a pure crystalline perovskite phase. There is a limiting factor that prevents the formation of perovskite phase for a specific selection of materials. This factor is so-called Goldschmidt tolerance factor. This factor relies on a simple geometrical approach to understand the prediction and stability of ionic solid-state structures[26]. This method assumes the constituent's ions as hard spheres whose radii can be calculated with good precision. By calculating the ratio of ionic radii, one can predict if these elements with a particular size can pack together in a crystal structure. Considering the perovskite structure of ABX_3, where A and B are cations and X is an anion, the tolerance factor can be expressed by the following formula

$$\frac{r_A + r_B}{\sqrt{2 * (r_B + r_X)}}$$

where:

r_A is the ionic radius of the A cation

r_B is the ionic radius of the B cation

r_X is the ionic radius of the X anion

This formula can be used to investigate whether the A cation can fit within the BX_6 octahedra. A value of tolerance factor of 1 means a good fit, where in the range of $0,8 \leq t \leq 1$ the perovskite structure can easily be formed. For the case of $t > 1$, the A cation is too big preventing the formation of perovskite phase. If $t < 0,8$ this indicates the A cation is too small promoting different non-perovskite structures to be formed[21]. **Figure 2-11** shows different perovskites formed after substituting the A cation or X anion [27,28].

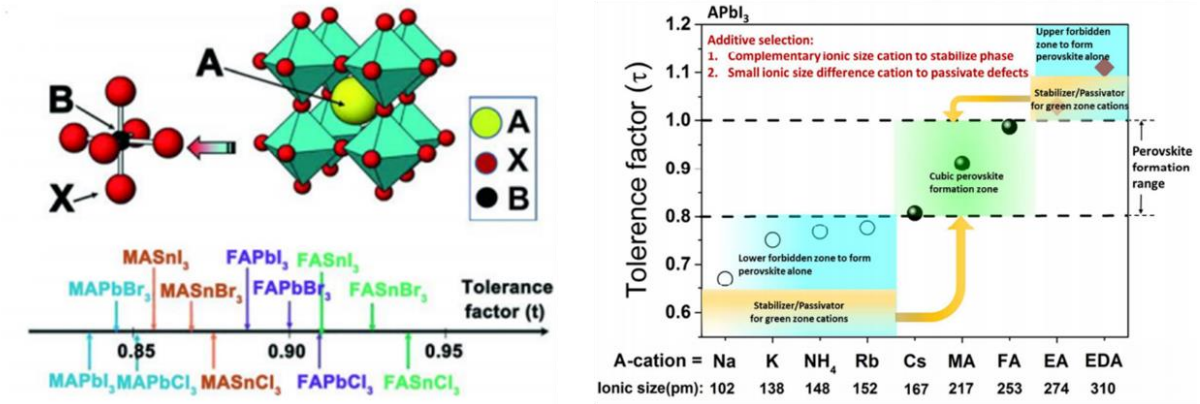

Figure 2-11 Different perovskites structures formed as predicted from the tolerance factor formula.

2.8 Characterization

To characterize a solar cell, some important photovoltaic parameters must be measured such as the power conversion efficiency, the open-circuit voltage, the short-circuit current, and the fill factor. The power conversion efficiency of a solar cell is defined as the ratio of energy output from the solar cell to input energy from the sun. In other words, it is the number of electrons per unit time per unit area that are collected by the respective electrodes. It can be measured by performing a so-called I-V measurement. In an I-V measurement a bias voltage is fed to the cell and current is measured as the bias voltage is being increased. The measurement curve tells directly the short-circuit current (I_{sc}) when bias is zero and the open-circuit voltage (V_{oc}) when the measured current is zero. The acquired short-circuit current is then divided by the electrode area, which is the actual active area of the solar cell. This is called the current density and the most commonly used unit for it is mA/cm^2. Also, the maximum power point is easily obtained from such a curve it being the point where the absolute value of the product of current and voltage is the highest. The short-circuit current (I_{sc}) and the open-circuit voltage (V_{oc}) are the maximum current and voltage respectively from a solar cell. However, at both of these operating points, the power

from the solar cell is zero. The "fill factor", more commonly known by its abbreviation "FF", is a parameter which, in conjunction with V_{oc} and I_{sc}, determines the maximum power from a solar cell. The FF is defined as the ratio of the maximum power from the solar cell to the product of V_{oc} and I_{sc}. Graphically, the FF is a measure of the "squareness" of the solar cell and is also the area of the largest rectangle which will fit in the IV curve (**Figure 2-11**). **Figure 2-12** shows an example of an I-V curve. The power conversion efficiency can be determined by the formula:

$$\boldsymbol{PCE\% = \eta = \frac{Isc * Voc * FF}{Pin}}$$

where Pin is the input power [15].

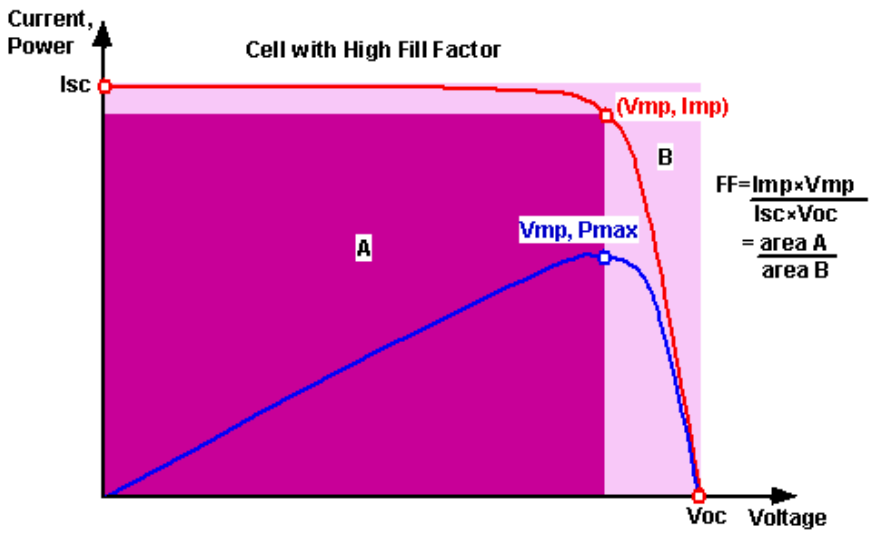

Figure 2-11 Graph of cell output current (red line) and power (blue line) as function of voltage. Also, the short-circuit current (I_{sc}) and open-circuit voltage (V_{oc}) points are shown, as well as the maximum power point (Vmp, Imp) [15]

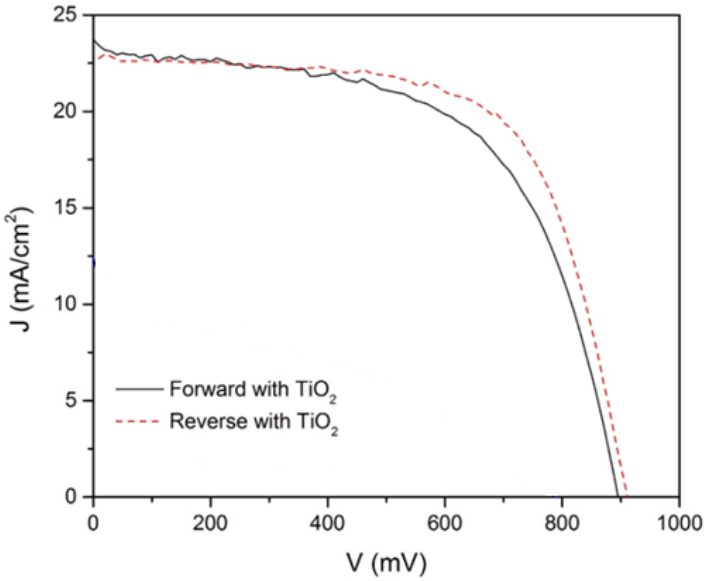

Figure 2-12 A processed I-V curve which shows the operation of a solar cell[14].

When determining the PCE the irradiance of the incident light is set to be 100 $\frac{mW}{cm^2}$, as this value corresponds well to the average power of sunlight on earth at middle latitudes and average conditions on which the cells will be used once perfected for commercial production and it is known as AM 1.5. AM stands for air mass and $\boldsymbol{AM} = \frac{\mathbf{1}}{\mathbf{cos}(\boldsymbol{\theta})}$, where θ is the angle of the sun from its zenith. AM 1.5 is standard according to which most solar cells are tested nowadays[29].The characteristics listed above (I_{sc}, V_{oc}, P_{max}, PCE, FF) are the most important and most commonly reported characteristics, but there are other interesting ones that can be derived from the same I-V measurements. External Quantum Efficiency (EQE) is the ratio of the number of carriers collected by the solar cell to the number of photons of a given energy incident on the solar cell and is given by the following equation

$$EQE = \frac{hc}{q}\frac{Jsc(\lambda)}{P(\lambda)\lambda^2}$$

where

h = Planck's constant,

c = the speed of light,

q = the elementary charge, λ is the wavelength

P(λ) = the incident optical power at a given wavelength.

Internal Quantum Efficiency (IQE) can be calculated from this by taking loss factors into account. Shunt Resistance is a desired characteristic of a solar cell. If shunt resistance is small, then fill factor is likely to be bad as well. When shunt resistance is small a significant part of the charge carriers finds a shorter shunt pathway thus avoiding the actual cell and reducing the cell's efficiency. A poor shunt resistance is most often due to manufacture defects rather than poor cell design [15].

2.9 Hybrid Perovskite properties

The $CH_3NH_3PbI_3$ and $CH_3NH_3PbI_{3-x}Cl_x$ perovskite have some advantageous properties which make them good candidates for photovoltaic applications. Some of the properties are described below:

- Strong optical absorbance near the band gap[19]
- The electron-hole diffusion length is greater than 1µm for a typical $CH_3NH_3PbI_3$ absorber[19].
- The absorption coefficient is higher than that of GaAs, an indication that thin film of about 500 nm can be effectively used [30].
- The band gap of 1,6 eV of the $MAPbI_3$ perovskite is very close to the ideal band gap of 1,34 eV predicted by Shockley–Queisser limit for a single junction solar cell [31] (**Figure 2-13)**.
- The ability to tune the band gap and the potential in tandem applications with other photovoltaic technologies [32]

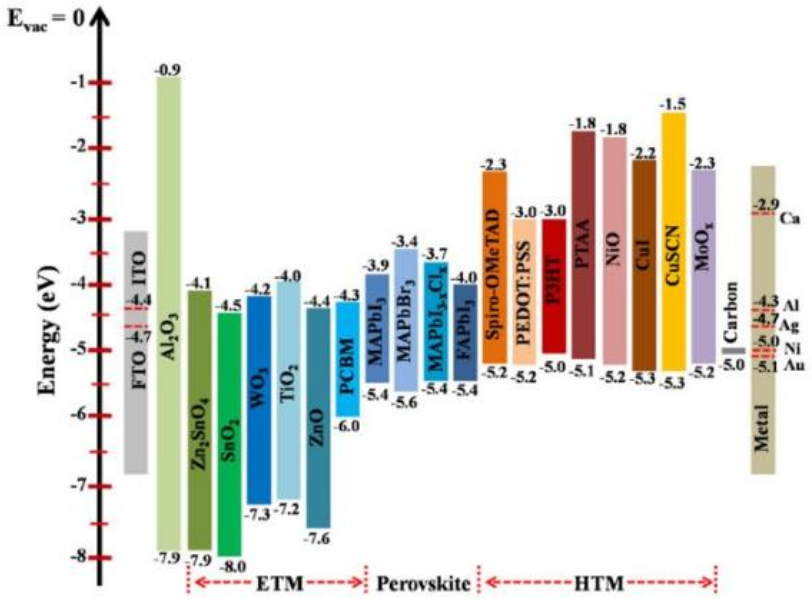

Figure 2-13 Energy diagram which shows the band gap of $MAPbI_3$ and $MAPbI_{(3-x)}Cl_x$ perovskites among with the energy levels of other HTL and ETL materials [33].

2.10 Advantages and disadvantages in perovskite solar cells

2.10.1 Advantages

- **Tunable band gap**

  Perovskite materials have tunable optoelectronic properties due to the simple perovskite chemistry. For example, a tunable band gap between 1.48 and 2.23 eV can be obtained by replacing the methylammonium cation in perovskite with a slightly larger formamidinium cation[34].

- **Strong optical absorption**

  Large absorbance coefficients in the visible region exhibit in $CH_3NH_3PbI_3$ perovskite due to its direct band gap as shown in **Figure 2-14**[35]

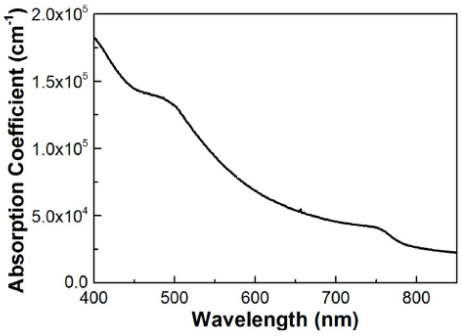

Figure 2-14 The absorption coefficient of $CH_3NH_3PbI_3$ [34]

- **High electron, hole mobilities and diffusion lengths**

  One of the most impressive characteristics of the perovskite is the high carrier mobility and relatively high diffusion length. Due to the lack of deep trap-states carrier mobility and diffusion length are reported with values of 2-66 $cm^2\ V^{-1}\ s^{-1}$ and 0.1-1.9µm respectively[19].

- **Free photo-generated carriers**

  Exciton binding energy is a key parameter to generate photovoltaic in perovskite solar cells. In $CH_3NH_3PbI_3$ the exciton binding energy has been reported ~37meV and therefore it is comparable with the thermal energy at room temperature (k_BT=26meV). Consequently, perovskites are non-excitonic materials and can generate free carriers upon illumination[22].

- **Large scale production**

  The fact that perovskite solar cells are easily reproducible due to the solution-based method and the low cost of the used material makes feasible a large-scale production.

2.10.2 Disadvantages

- **Toxicity**

  A perovskite solar cell uses Pb (lead) as a main material for its synthesis and this is one of the breakdown products of perovskite. This is known to be toxic and there are concerns that it may be carcinogenic. Also, lead is a massive pollutant for the environment. Therefore, during the fabrication of perovskite solar cells, lead precursors must be treated with caution in order to prevent health hazards and environmental pollution.

- **Hysteresis**

  Hysteresis behavior in forward and reverse direction has been observed in perovskite solar cells in current versus voltage dependence (**Figure 2-15**). Several explanations have been proposed for this behavior including ferroelectricity, accumulation of charges at grain boundaries, filling of surface trap states, dipole rearrangement and ionic migration[36].

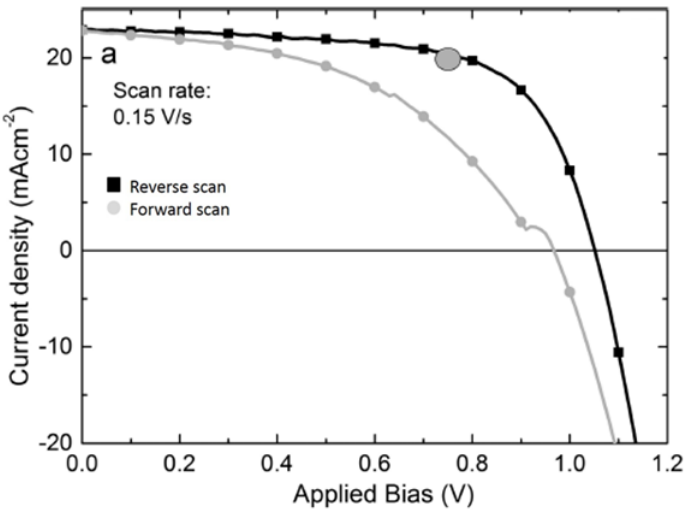

Figure 2-15 The hysteresis phenomenon observed after a J-V measurement[36].

- **Decreased stability**

  Perovskite solar cells suffer from extreme instability when interact with water, heat and light. This is due to the instability of both perovskite material itself as well as the transport materials used in the device architecture. The perovskite film is sensitive to moisture because of the hygroscopic amine salt makes the device highly prone to rapid degradation in moist environments[37]. Furthermore, ETL, eg. PCBM and HTL, eg. PEDOT:PSS also cause the instability. For example PCBM layer is not stable in air and PEDOT:PSS has acidic nature (pH∼2) affecting the stability of device[38].

3. Experimental

In the following section, preparation and fabrication of the inverted structure perovskite solar cell is described. To fabricate a solar cell, one has to go through several processes such as cleaning substrates, annealing, spin coating, and evaporation. All the methods are discussed in detail below.

3.1 Equipment

- **Sonicator**

Ultra-sonication is required for the cleaning of substrates. In this process sound energy (acoustic waves) is applied (200-400 kHz) to a container where a solvent and the substrates are placed. The solvent is usually water. This phenomenon creates rapid vibrations around the substrates that remove most of the contaminants such as dust, dirt (etc)[39]. In this work Elma Sonicator by Elmasonic was used (**Figure 3**).

Figure 3 Sonication system by Elmasonic

- **UV ozone**

Ultraviolet ozone treatment is a subsequent method of cleaning the substrates. The specific method aims to remove the organic contamination and increase the surface hydrophilicity to deposit a uniform layer afterwards. This effect is caused by irradiating the surface of a substrate with suitable lamps that emit ultraviolet light at wavelengths of 185 nm and 254 nm[40]. It is a photo-sensitized oxidation process by atomized oxygen and high reactive ozone. The UV ozone cleaner that was used is a MB-UV-O3-Cleaner by MBRAUN (**Figure 3-1**).

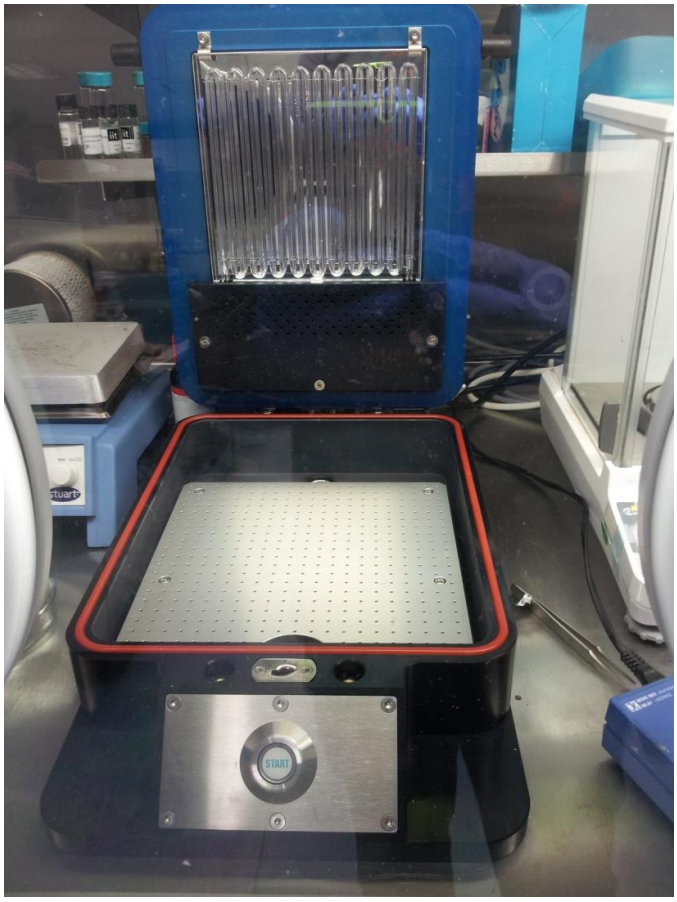

Figure 3-1 The UV ozone cleaner system in a glove box

- **Spin coater**

Spin coating is the process where a uniform thin film is deposited on a flat substrate by coating a solution of the desired material in a solvent while it is rotating. The rotation of the substrate at high speed (>600rpm) means that the centripetal force combined with the surface tension of the solutions of the solution pulls the liquid coating into an even covering (**Figure 3-2**)[41 42]. During this time the solvent then evaporates to leave the desired material on the substrate in an even coverage. Two spin coaters were used, the MB-SC-200 by Ossila (in glove box) and the WS-650-23 by Laurell (**Figure 3-3**).

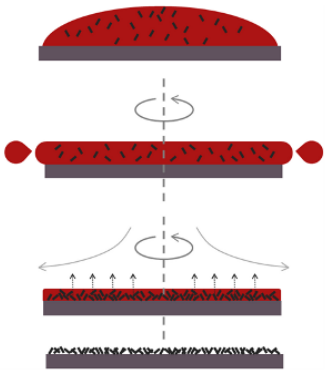

Figure 3-2 Schematic representation of the spin coating a small molecule in solution [45].

Figure 3-3 The WS-650-23 by Laurell (left) and the MB-SC-200 by MBraun (right) spin coater

- **Glove box**

Glove box is a sealed container designed to allow one to manipulate objects where an inert atmosphere is desired. Typically, a glove box is filled with nitrogen, an inert gas which is used to avoid unwanted chemical reactions degrading a sample. Furthermore, the inert gas in a glove box is pumped through a series of devices which remove vapors of solvents, water and oxygen from the gas. All above make the glove box a high purity inert atmosphere container, suitable for manipulating materials which are sensitive to oxygen and water molecules[43]. A MB-200B Modular glove box work station was used by MBRAUN (**Figure 3-4**).

Figure 3-4 The MB 200B glove box system by MBRAUN

- **Evaporator**

Thermal evaporation is a method of thin film deposition. The solid material is heated in a high vacuum chamber, reaching a melting point temperature where it produces some vapor pressure. The vapor stream of the evaporated material traverses the chamber to reach the substrate and make a coating. The high vacuum is required so that the evaporated particles can travel directly to the substrate without colliding with the background gas. Once the particles reach the substrate, they condense back to solid

state forming a compact thin film (**Figure 3-5**) [44 45]. The MB-EcoVap by MBRAUN evaporator system was used (**Figure 3-6**).

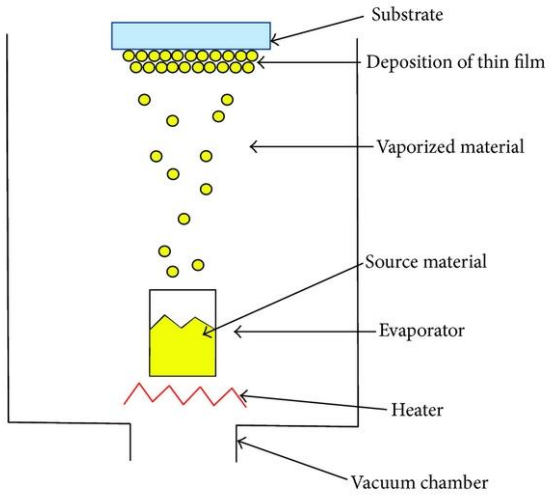

Figure 3-5 The evaporated particles travel to substrate[45].

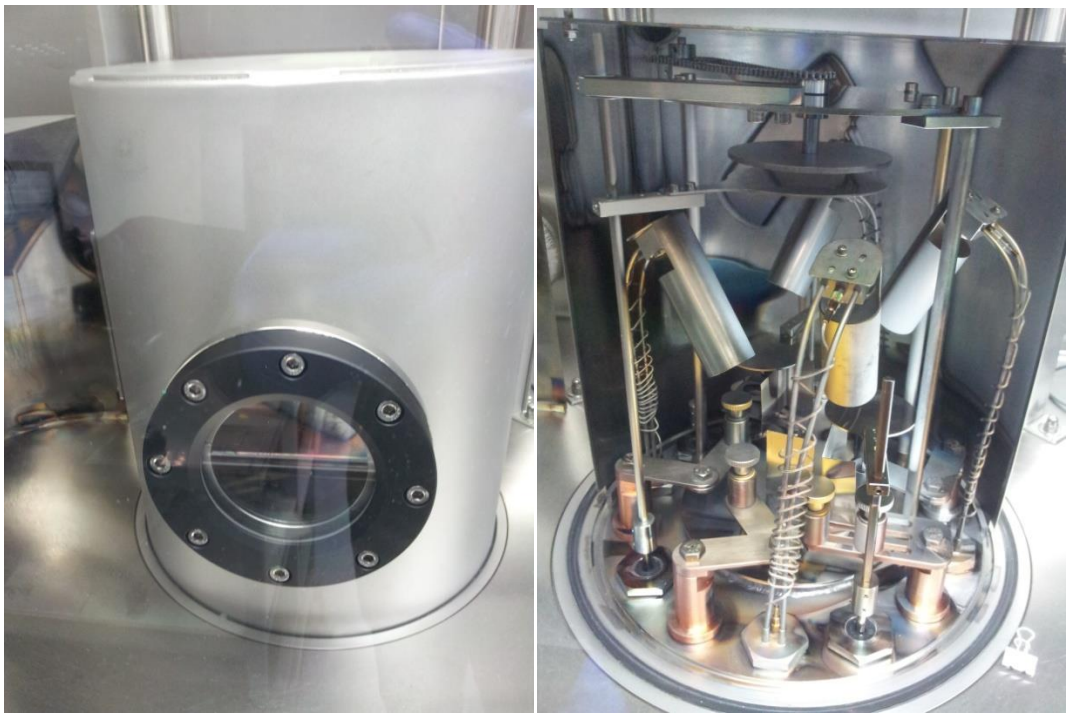

Figure 3-6 The MB-EcoVap evaporator under high vacuum (left) and with the vacuum chamber open (right).

- **Ultraviolet-Visible spectroscopy (UV-Vis)**

UV-Vis spectroscopy is a method that can be used to determine the wavelength of light, in the ultraviolet or the visible region of the electromagnetic spectrum that is absorbed by a molecule. A UV-Vis spectrophotometer emits light with a range of wavelengths from 200nm to 800nm through a sample and measures the intensity of light reflected/transmitted from a sample, compared to the intensity of light reflected/transmitted from a reference material such as a glass substrate. The corresponding absorption spectrum shows the wavelengths that the sample absorbed. A color of a sample can be explained by this method. For example, if a sample has green color, then it absorbs the complementary of green which is red. This method is based on the principle of electronic transition in atoms upon absorbing suitable energy that allows electrons to excite from a lower energy state to higher energy state. Since the absorption spectrum reveal information on electronic transition, the onset of absorption is considered as the optical band gap of semiconductors or conjugated polymers[46]. **Figure 3-7** gives an example of how the bad gap is determined of P3HT an organic charge transport layer[47].

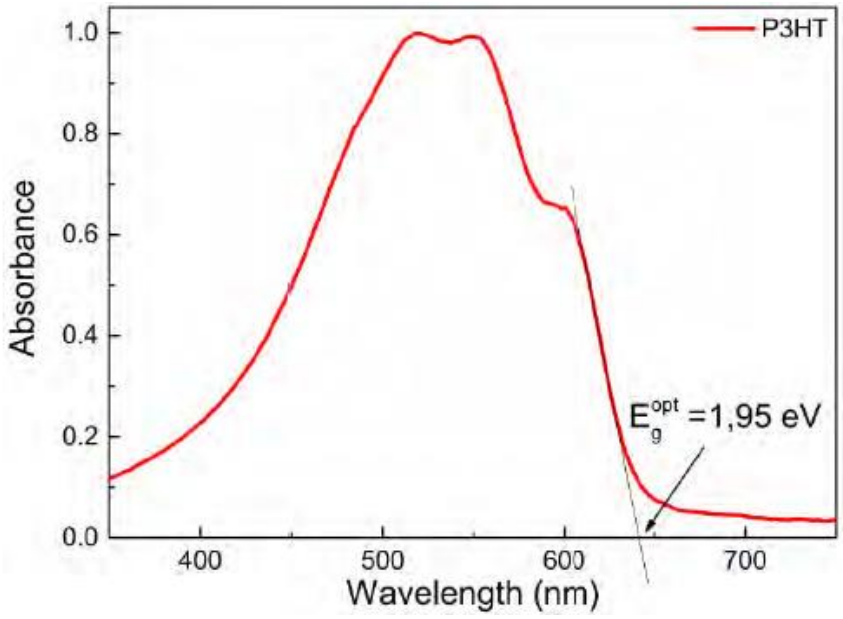

Figure 3-7 The determination of band gap of P3HT[47].

- **X-Ray Diffraction**

X-rays are electromagnetic waves with wavelength ranging from 0,01nm to 10nm. When X-ray photons hit a crystal, the atomic and molecular structure of that crystal can be identified. The atoms of the crystal will scatter X-ray waves and constructive interference from multiple scattering signals will be occurred in specific conditions. The whole phenomenon is described by Bragg's law.

$$\boldsymbol{2\,d\,sin\theta = n\,\lambda}$$

Where d is the spacing between diffracting planes, θ is the incident angle, n is an integer number and λ is the wavelength. The distance is inverse proportional to the scattering angle. In other words, small repeating distances will refract to larger angles. By that the distance between ordered molecules can be determined. **Figure 3-8** shows an illustration of X-ray diffraction by a crystal[48].

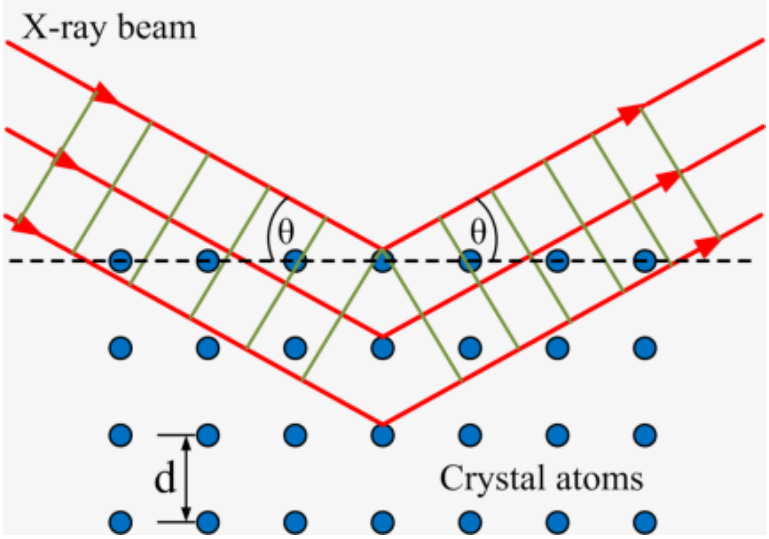

Figure 3-8 X-ray diffraction by a crystal [49]

- **Solar simulator**

A solar simulator is an apparatus that provides illumination approximating natural sunlight. The purpose of the solar simulator is to provide a controllable indoor test facility under laboratory conditions, used for testing solar cells, sun screens and other types of materials and devices. A solar simulator attached to the bottom of the glove box was used (**Figure 3-9**)[50].

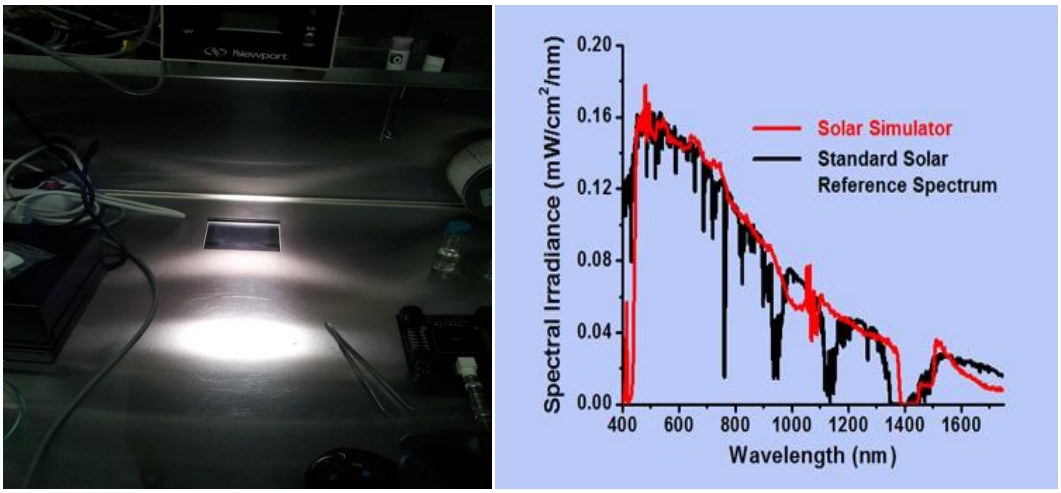

Figure 3-9 Solar simulator irradiating white light and the corresponding spectrum compared to sunlight[51].

- **SEM**

Scanning electron microscope (SEM) is a type of electron microscope that produces images of a sample by scanning it with focused beam of electrons. The electrons that are emitted interact with the atoms of the sample and subsequently generate signals regarding to the surface topography. The SEM analysis requires vacuum and conductive samples are preferred[52].

- **Quantum efficiency (Q.E)**

Quantum efficiency represents the ratio of numbers of carriers that are extracted from the solar cell to the number of photons of a given energy incident on the solar cell. The quantum efficiency can be given as a function of wavelength or energy. That kind of measurement indicates the amount of current that the solar cell will produce illuminated by photons of a particular wavelength. As a result, one can evaluate the amount of current density (J_{sc}) that the cell will produce[53]. For characterizing the solar cells, QE-T quantum efficiency setup by EnliTech was used (**Figure 3-10**).

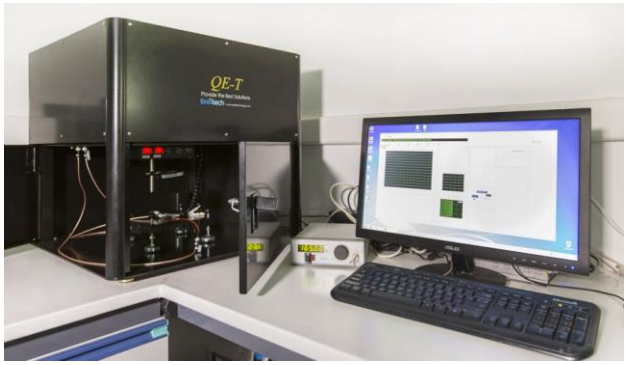

Figure 3-10 The quantum efficiency measurement system setup.

- **Atomic Force Microscopy (AFM)**

Atomic Force Microscope (AFM) is useful tool to study the morphology and thickness of thin films. The instrument consists of a cantilever which has a sharp tip in order of nanometers attached to it. The tip will interact with the sample by electrostatic, van der Waals or capillary forces. The cantilever is attached to a piezoelectric material which is used for adjusting the position of the tip upon scanning. These forces shall deflect the cantilever according to Hooke's law. A laser beam is reflected back off the cantilever which is then collected by sensitive detector. Upon scanning a sample, the cantilever would deflect when hitting features (peaks or valleys) thus the detector will receive a different signal providing information for the morphology of the sample [54]. For the characterization of film morphology, AFM setup by Park Systems was used.

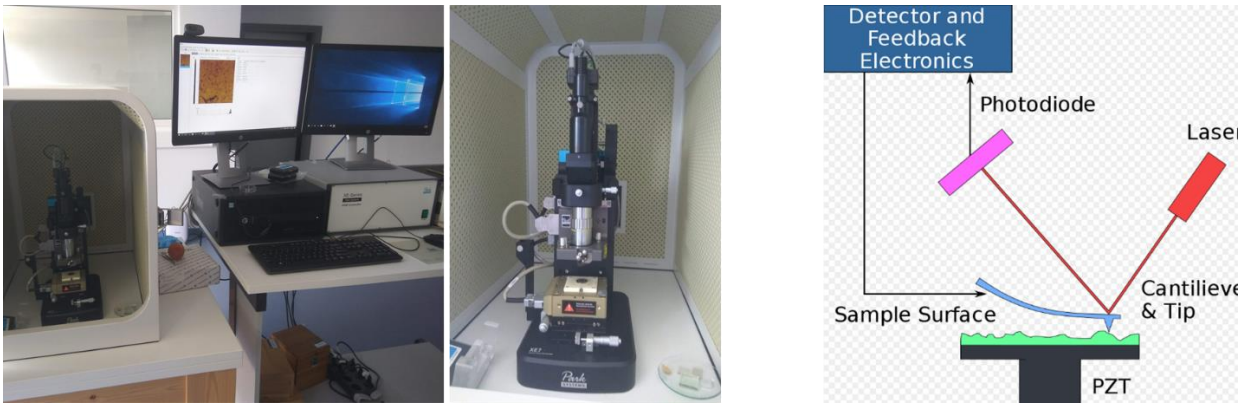

Figure 3-11 AFM setup by Park Systems (left) and fundamental principal of the measurement (right).

3.2 Materials

All the materials that were used to fabricate a perovskite solar cell are listed below.

- $PbCl_2$ and PbI_2 precursor with molecular weight of 287,11 g/mol was purchased from Sigma-Aldrich
- Methylammonium iodide (MAI) precursor with molecular weight of 158,97 g/mol was purchased from Dyesol
- Poly(3,4-ethylenedioxythiophene) polystyrene sulfonate (PEDOT:PSS) with electrical conductivity of 1000 S/cm^2 was purchased from Heraeus Clevios 4083
- PTAA polymer with polydispersity of 2,53 was purchased from Solaris Chem
- Glass substrates with Indium Tin Oxide electrode with resistance of 20 Ω/sq were purchased from Naranjo Substrates
- $PCBM_{60}$ [6,6]-phenyl-C61-butyric acid methyl ester (>99.9%) with molecular weight of 910,88 g/mol was purchased from Solenne BV.
- Dimethylformamide (DMF) (>99.8) with molecular weight of 73,09 g/mol was purchased from Sigma-Aldrich
- PFN with molecular weight Mw= 50-250kD was purchased from Solaris Chem
- Al pellets were purchased from Kurt J. Lesker

3.3 Experimental process

In this section, the deposition techniques that took place are described. Different conditions and additives were tested to achieve the best PCE and morphology. All methods are described in detail below.

Preparation methods

- **Cleaning the substrates**

To fabricate a solar cell, first the glass/ITO substrates must be cleaned. This was achieved using ultrasonic bath with deionized water, acetone and isopropanol for 10 minutes each. After sonication the substrates were taken to a drying oven at 120°C for 20 minutes. The next step of cleaning is the ultraviolet ozone treatment. The substrates were taken into the ultraviolet ozone cleaner for 15 minutes (**Figure 3-11**).

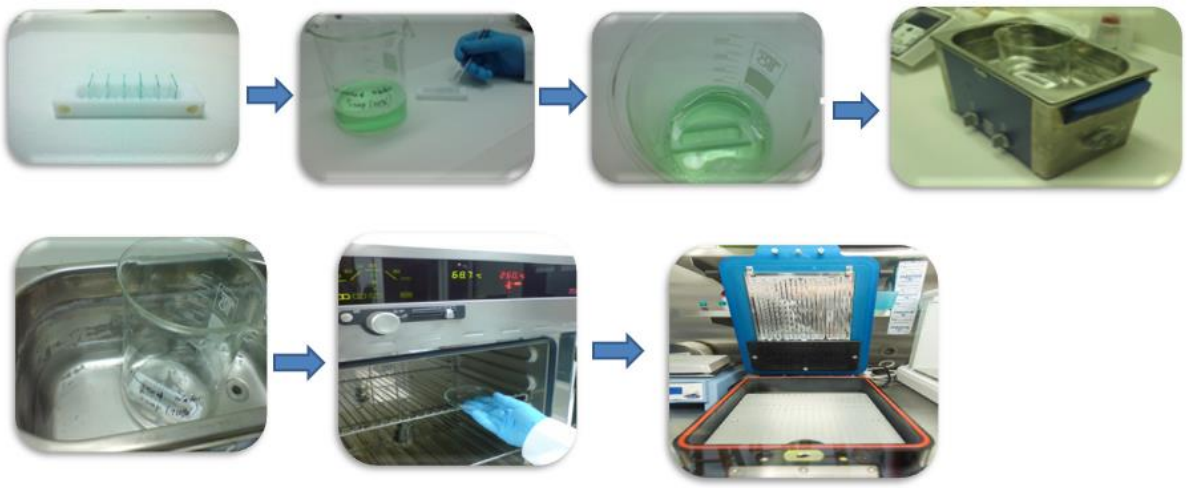

Figure 3-11 The cleaning process of substrates.

- **Preparation of $CH_3NH_3PbI_{(3-x)}Cl_x$ perovskite**

To synthesize the mixed halide perovskite, the precursors must be mixed in a glove box with nitrogen atmosphere. More specifically 763,1 mg of MAI and 444,9 mg $PbCl_2$ are mixed in 2ml DMF solution (molar ratio 3:1). The precursor solution was stirred for 2 hours at 70°C.

- **Preparation of $MAPbI_3$ perovskite**

For methylammonium lead triiodide perovskite, the preparation has two steps. First PbI_2 was dissolved in DMF with a concentration of 450mg/ml and was heated at 70°C for 12 hours. Afterwards MAI solution is prepared by dissolving 45mg MAI in 1ml of 2-propanol. The MAI solution was stirred at 50°C for 12 hours as well.

- **Preparation of $PCBM_{60}$**

To prepare the ETL solution, 20 mg of $PCBM_{60}$ were dissolved in 1ml of anhydrous chlorobenzene and stirred at 70°C for 12 hours.

- **Preparation of PTAA**

For the HTL solution, 12mg of PTAA were dissolved in 1ml of toluene. The solution was stirred at room temperature for 12 hours.

- **F4-TCNQ preparation**

To prepare the F4-TCNQ solution, first an optimization for the PTAA took place. Once the optimized concentration was found, different concentrations of F4-TCNQ were tested in order to achieve the best efficiency. The doping of PTAA with F4-TCNQ was performed by weight ratio. The F4-TCNQ solution was dissolved in toluene and stirred at 70°C for 12 hours.

Deposition of HTL, perovskite, ETL and counter electrode

- **PEDOT:PSS deposition**

After cleaning the substrates, deposition of PEDOT:PSS took place. The PEDOT:PSS solution is stored at temperatures between 5-10^{o}C. Reaching room temperature, the PEDOT:PSS solution was first filtered through a 0,45μm PVDF filter and then spin-coated onto ITO substrates at 4000 rpm for 60 seconds (**Figure 3-12**). Using the above spin coating conditions, the resulted layer was about 40nm. A small area was cleaned from the ITO surface using a swab dipped into deionized. After that the substrates were taken to a drying oven for 20 min at 120^{o}C to evaporate the solvent.

- **PTAA deposition**

Before the deposition of the HTL, the solution was filtered through a 0,45μm PTFE filter. The PTAA solution was spin-coated onto the ITO substrates at 6000 rpm for 30 seconds. The thickness of PTAA was about 50nm. Afterwards a small area of the film was cleaned using a swab dipped into CB. The substrates were then annealed on a hotplate at 110^{o}C for 10 minutes.

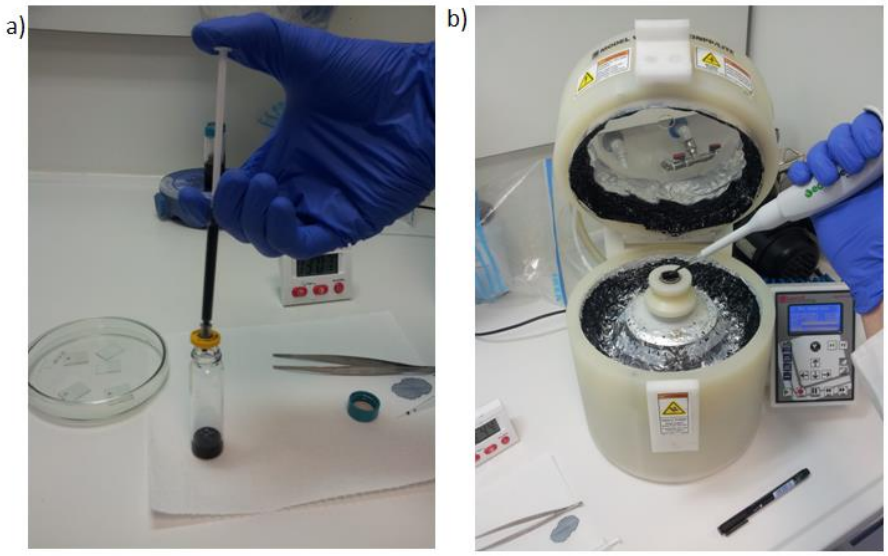

Figure 3-12 a) Filtering PEDOT:PSS with a PVDF filter b) Spin coating the PEDOT:PSS

- **Perovskite deposition**

Afterwards, the substrates were transferred into the N_2 glovebox for the perovskite precursor deposition. Before use, all the perovskite precursor solutions were filter through a 0,45μm PTFE filter. The $CH_3NH_3PbI_{(3-x)}Cl_x$ precursor solution was spin-coated onto the PEDOT:PSS layer at different revolutions per minute (rpm) ranging from 2000 to 4000 rpm. Then the substrates were placed on a hot plate at various temperatures and annealing times. The annealing temperature and time was ranging from 90min to 210min and 90°C to 100°C respectively as stated in the literature [56, 57, 58, 59, 60]. Again, a little area was cleaned this time using a swab dipped into DMF. The cleaning process took place during the thermal annealing of the perovskite.

For the $MAPbI_3$ perovskite, first a hot solution of PbI_2 was spin-coated onto the HTL covered substrate at different revolution per minute ranging from 2000 to 6000 rpm. The substrates were heated at 100°C for 10 minutes. After that the substrates were left to cool down to room temperature. Next the MAI solution was spin-coated on the PbI2 film at different rpm ranging from 2000 to 6000. The substrates were then heated at 100°C for different annealing times ranging from 30 to 90 minutes.

$PCBM_{60}$ deposition

A PCBM solution with concertation of 1.3 wt% in chlorobenzene was spin coated at 2000 rpm on top of the perovskite layer. This time the area was cleaned using a swab dipped into chloroform. The substrates were covered in a petri-dish and dried at room temperature for 30 minutes.

PFN deposition

After the deposition of the ETL, PFN solution was spin coated on the substrates at 2000 rpm. A final step of cleaning was performed before the deposition of Al electrode.

Al electrode deposition

Finally, to complete the device, the cathode electrode must be deposited on top of all layers. The deposition of aluminum was performed by thermal evaporation under vacuum ($1x10^{-6}$ mbar) with rate of 1,5 Å per second. A shadow mask was used to define an active area of $0,4cm^2$.

Cleaning process for each of the layers took place exactly after coating to keep an open area on the ITO pattern for electrical measurements. This way the ITO electrode would not be affected by any residual. **Figure 3-13** shows the schematic representation of device fabrication and the cleaning process and **Figure 3-14** shows the cross section of the complete device.

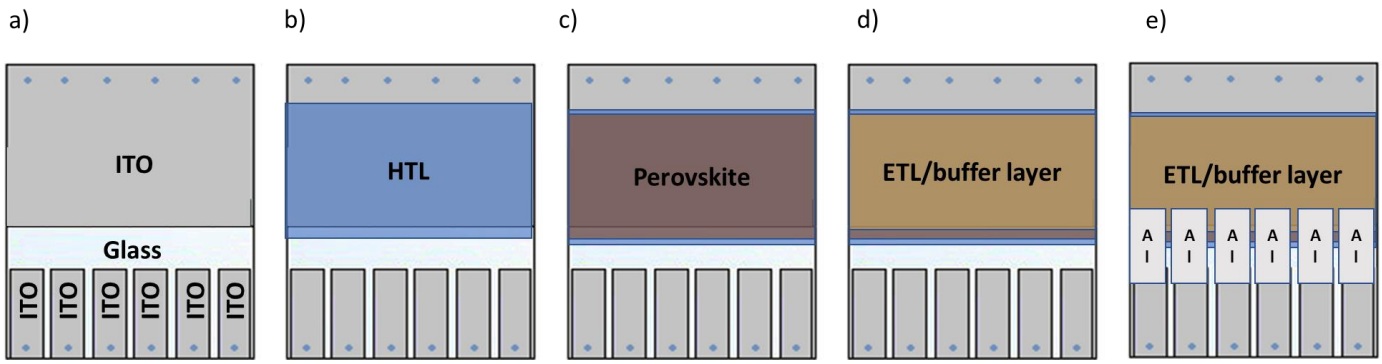

Figure 3-13 a) Glass/ITO substrate b) deposition of PEDOT:PSS c) deposition of Perovskite d) deposition of PCBM and PFN e) deposition of Al electrodes.

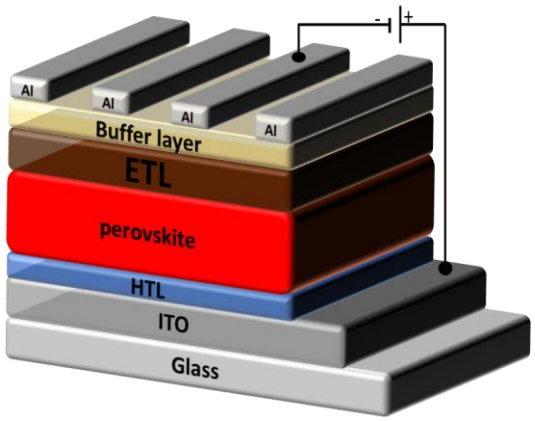

Figure 3-14 Schematic cross section of the device.

3.4 Characterization

To characterize the solar cells, the J-V characteristics were measured by an Agilent B1500 Semiconductor Device Analyzer. The solar cell performance was tested with an Air Mass 1.5 Global (AM1.5 G) and the irradiation intensity was 100 mW cm^2. The scan rate was 17 mVs^{-1} and the active area was defined to be 0,4cm^2. The EQE measurements were obtained using a (Elitech QE-mini) system by applying monochromatic light from a xenon lamp (using a Diffraction grating monochromator) under ambient conditions. The monochromatic light intensity was calibrated using a Si photodiode and chopped at 100 Hz. Masks (1,70 mm^2) made of thin black plastic were attached to each cell before measurement of the J–V characteristics and the EQE to accurately measure the performance of solar cells (**Figure 3-15**).

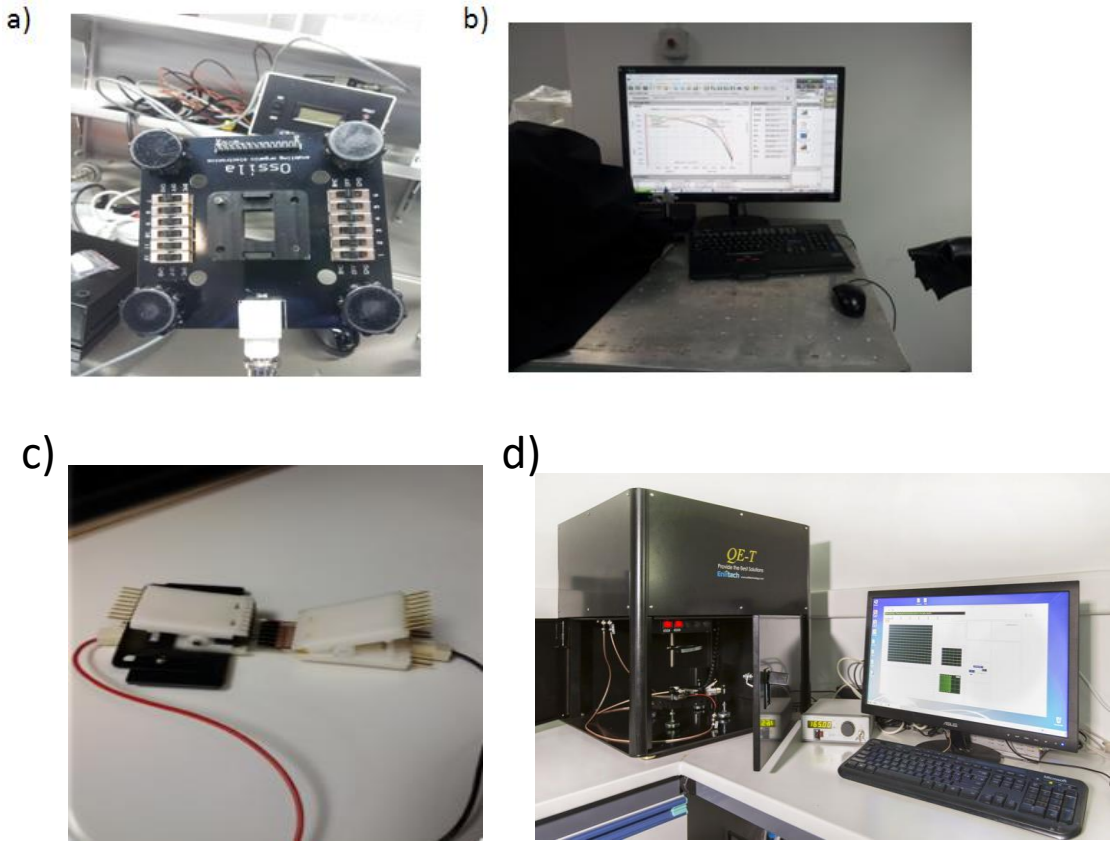

Figure 3-15 a) The plastic mask for the devices b) Measurement of J-V characteristics c) Contact of substrate electrodes by crocodiles d) Measurement of EQE

4. Results and discussion

In this section, the experimental results which obtained with the methods described in section three are presented and analyzed. The parameters that affected the morphology and the total performance of the cells are discussed.

4.1 Optimization of $MAPbI_{(3-x)}Cl_x$ mixed halide perovskite

To optimize a device based on the mixed halide perovskite, previously reported method based on the normal structure architecture was followed [61]. However, due to the fact that in the inverted structure a simplified and low temperature process can be used, this work was focused on the planar inverted architecture. A 50nm thin layer of PEDOT:PSS was deposited on top of the ITO substrate as a hole transport layer. On top of that about ~500nm of perovskite layer was spin coated at 2000 rpm. The annealing time for the perovskite layer was 150 minutes at 90°C and 20 minutes at 120°C. These conditions were found to be promising according to a previous project where a normal structure PeSC was fabricated [64]. On top of the perovskite about ~ 50nm layer of PCBM, and 100nm of Al was deposited to complete the device as described in the previous section (**Figure 4**)**.** However, in the inverted structure the specific method of annealing did not give the expected results. The respective photovoltaic characteristics are summarized in **Table 1**.

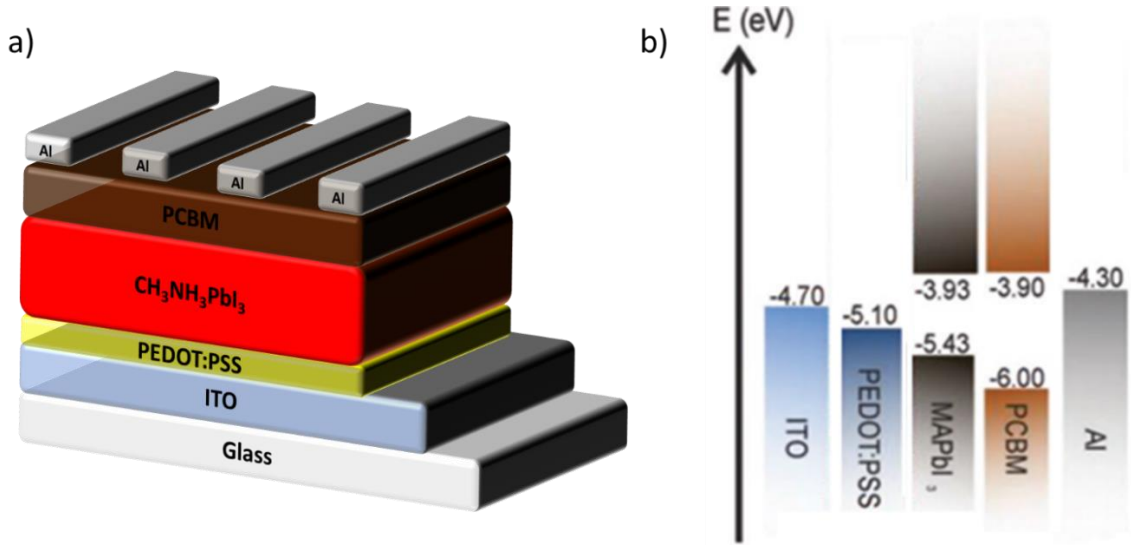

Figure 4-1 a) the complete device b) energy diagram of the device.

Table 1

J_{SC} (mA/cm^2)	V_{OC} (mV)	FF (%)	PCE (%)
7,1	693	31	1,56

The first device exhibits a very poor PCE of 1,56% possibly due to the unfavorable crystallization of the perovskite layer. To study the crystallinity and morphology of such film, XRD and SEM measurements would provide better insights. **Figure 4-2** shows the corresponding J-V curve.

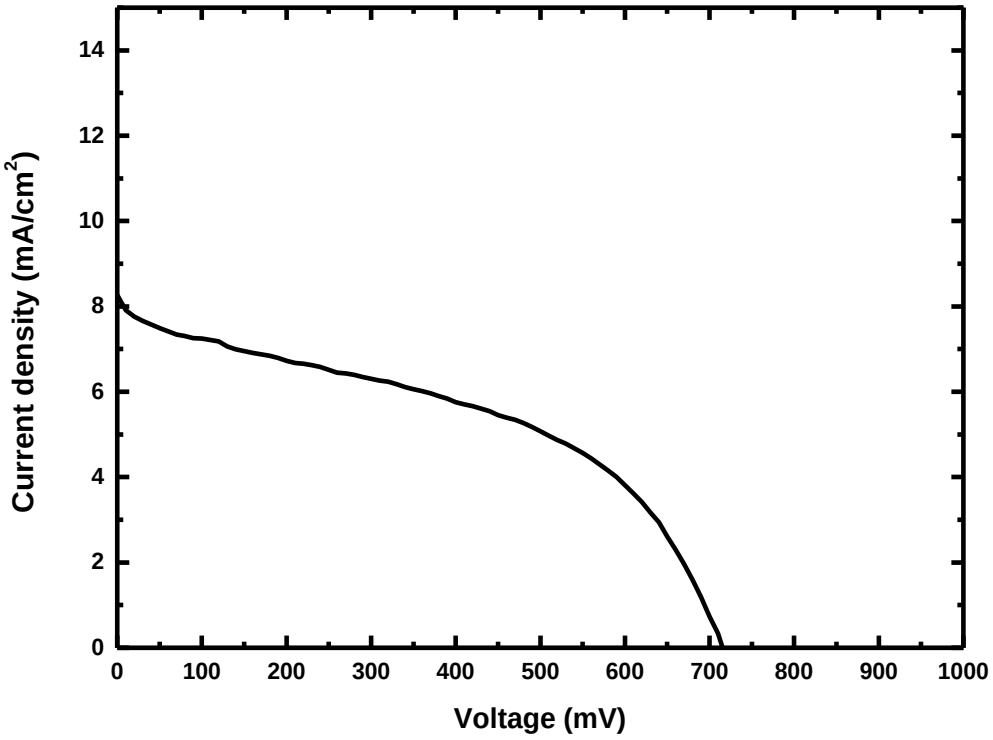

Figure 4-2 J-V curve of the first sample.

4.2 Annealing optimization

To enhance the photovoltaic characteristics of the device the fabrication process should be optimized. Thus, an annealing optimization was carried out to improve the crystallization of the perovskite layer and the performance of the perovskite solar cell. Different annealing times were tested by keeping the same spinning conditions (2000 rpm) and annealing temperature set at 100^{o}C. More specifically the annealing time was varied from 30 min to 110 min. **Table 2** shows the results of the temperature optimization where the best annealing time was found to be at 70 min. All the characteristics at the specific time were significantly enhanced compared to the previous experimental conditions. **Figure 4-3** shows the J-V curves that were recorded for each of the annealing temperatures. Also, the curve that corresponds to the optimized annealing temperature is better and has the appropriate shape approaching a square [15].

Table 2

Annealing time (min)	J_{SC} (mA/cm^2)	V_{OC} (mV)	FF (%)	PCE (%)
30	1,3	835	18	0,2
50	7,3	937	33	2,3
70	**13,8**	**847**	**42**	**5,0**
90	17,0	792	30	4,0
110	8,0	768	37	2,3

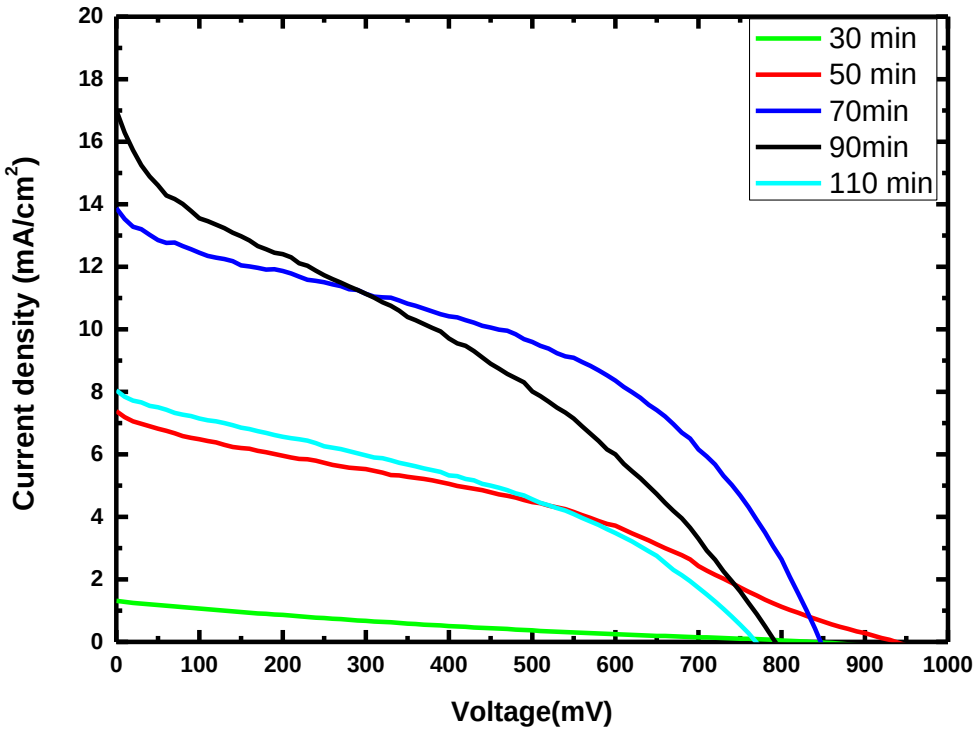

Figure 4-3 J-V curves of the optimization samples

4.3 Low reproducibility issue

Even though the performance was improved, the reproducibility of the devices was poor at the specific conditions (100°C/70 min/2000rpm). Each cell resulted in different PCE values as it can be observed in **Table 3**.

Table 3

	J_{SC} (mA/cm^2)	V_{OC} (mV)	FF (%)	PCE (%)
	13,4	904	39	5,0
	11,6	872	32	2,6
	7,7	916	38	5,2
	16,0	837	43	3,0
	12,0	900	41	3,7
	11,6	872	36	4,0
	12,3	843	35	2,1
	14,2	864	39	5,1
Mean value	**12,35**	**876**	**37**	**3,8**

One possible explanation could be the lack of uniformity and coverage of the perovskite film. As referred in the literature[62] a non-uniform layer of perovskite suffers from pinholes which create shunt pathways reducing the photovoltaic performance of the cell. That kind of pinholes allow the ETL and HTL layers to come in touch and affect the performance of the solar cell by causing short circuits. The non-uniform layer of perovskite was confirmed by SEM image of the respective sample as shown in **Figure 4-4 (b)**. The average size of the pinholes is quite big (about 1μm) which in this case would affect the performance and the reproducibility. XRD pattern is shown in **Figure 4-4 (a)**. The strong diffraction peaks at 14,69° and 29,05° correspond to the (110) and (220) planes respectively. These peaks indicate the tetragonal

perovskite structure phase formation. However, the peak at 20,69° corresponds to the presence of orthorhombic $PbCl_2$ crystal, an indication that the precursors did not fully react with each other. The non-transformation of the precursors to the final crystal structure of perovskite could reduce the device performance as the residual $PbCl_2$ would make the film porous and at the same time act as a recombination center [63].

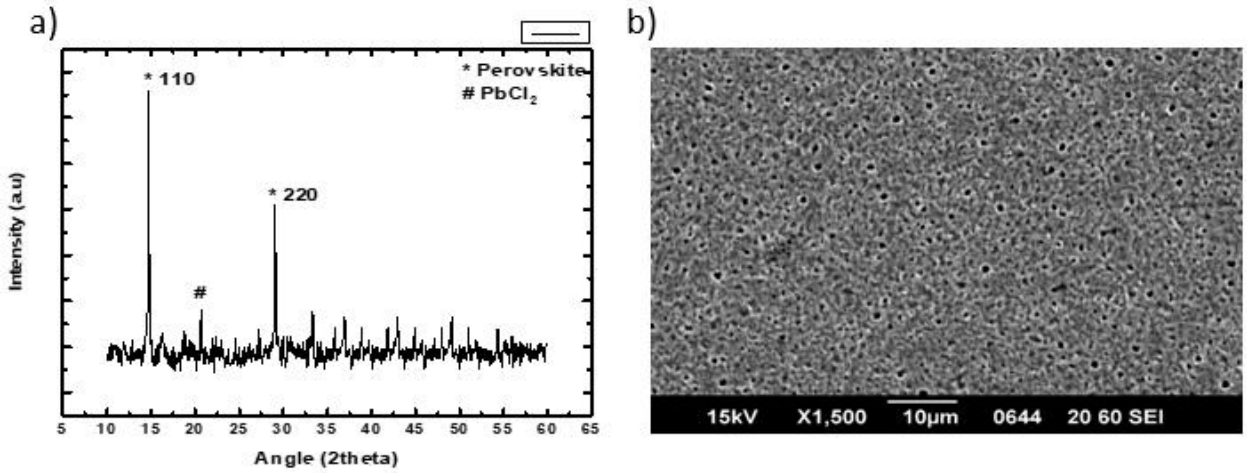

Figure 4-4 XRD pattern and SEM image of the sample. In the XRD pattern (*) indicate the two characteristic peaks which confirm a tetragonal perovskite structure and (#) indicates the unreacted $PbCl_2$.

To achieve better performance and reproducibility the deposition conditions of the perovskite were altered. On top of PEDOT:PSS layer the perovskite precursor was spun at different rpm (2000-5000) making in this way a thinner film. All the other deposition and annealing conditions were kept same. Upon testing, the performance increased to about 8,2% and the reproducibility was significantly increased. **Table 4 and 5** shows the results of the devices and the improvement in reproducibility.

Table 4

Perovskite (rpm)	J_{SC} (mA/cm^2)	V_{OC} (mV)	FF (%)	PCE (%)
2000	13,0	872	39	4,4
3000	16,4	864	47	6,7
4000	**18,2**	**870**	**52**	**8,2**
5000	19,0	830	49	7,7
6000	18,4	824	50	7,6

Table 5

	J_{SC} (mA/cm^2)	V_{OC} (mV)	FF (%)	PCE (%)
	17,1	875	49	7,3
	18,7	887	53	8,8
	17,4	863	50	7,5
	19,0	874	48	8,0
	16,9	854	54	7,8
	18,0	881	56	8,8
	17,8	873	55	8,5
	18,2	897	56	9,1
Mean value	**18,5**	**875**	**52**	**8,4**

This improvement was attributed mainly to the reduction of the pinholes that possibly indicates a better crystallization of the thinner perovskite films during the annealing process. **Figure 4-5 (b)** illustrates the SEM picture of the thinner perovskite layer and significantly improvement can be seen. The film is much smoother with fewer and smaller pinholes corresponding to higher PCE and better reproducibility. XRD pattern in **Figure 4-5(a)** shows a fully crystalline perovskite phase and no other picks from the residual precursors were identified. This is an indication that the thinner perovskite layer was required to achieve better reproducibility and device performance. UV-vis absorption and photoluminescence spectra shown in **Figure 4-6** confirming the formation of mixed halide perovskite with a band gap of 1,6 eV.

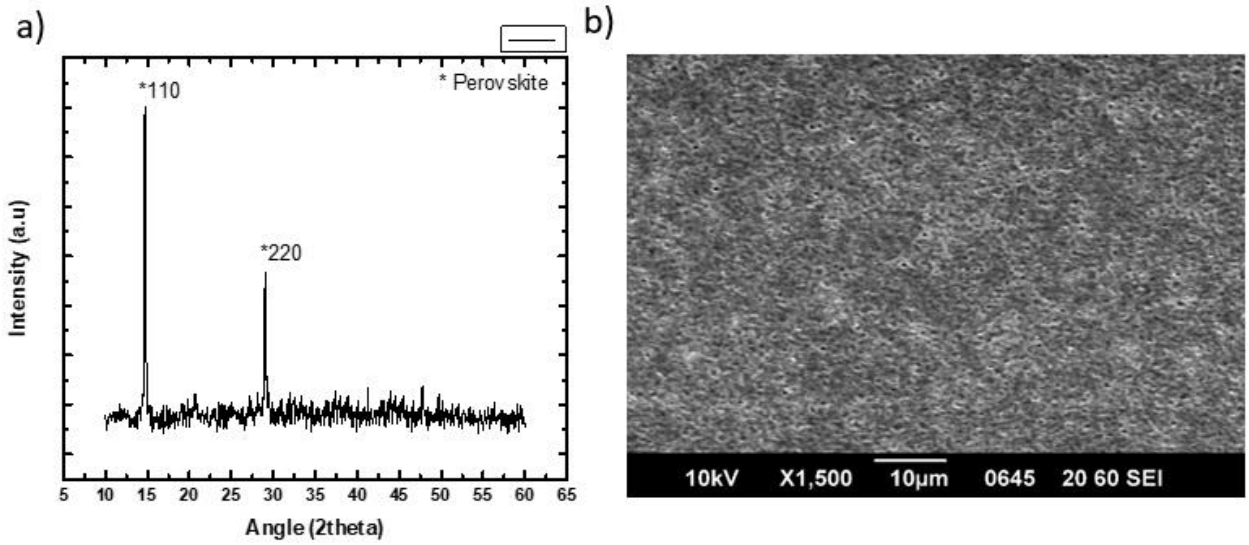

Figure 4-5 XRD pattern and SEM image of the thinner perovskite layer. In the XRD pattern there is no peak for unreacted $PbCl_2$ which confirms the full reaction of the precursors.

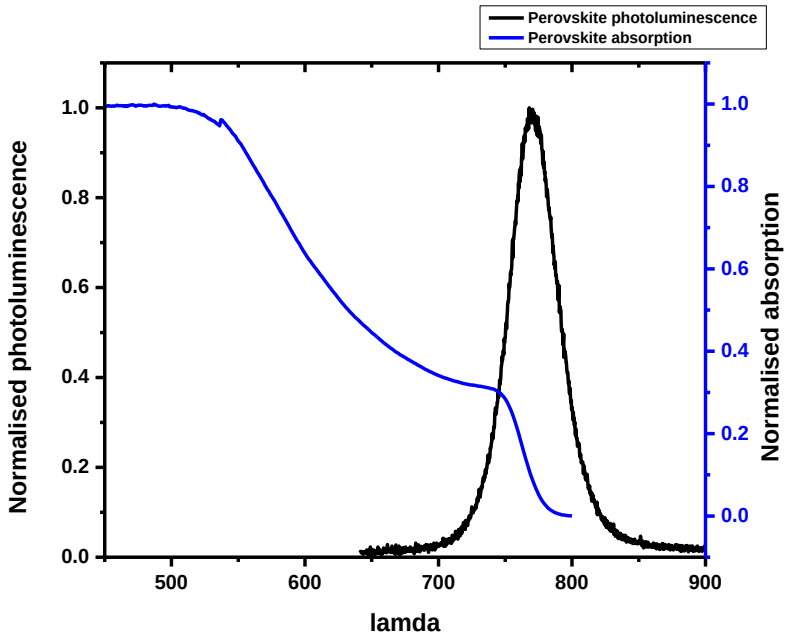

Figure 4-6 Photoluminescence and absorption spectra of the mixed halide perovskite

4.4 Introduction of PFN

As it was shown by previous studies, the PCBM60 layer might not form a compact film thus failing to form an ideal ohmic contact with the silver electrode. Hence, direct contact between perovskite and the metal counter electrode might occur forming a Schottky barrier which reduces the device performance. Different studies have investigated the PCBM/metal interface reporting inclusion of additional layers such as Ca,[64] LiF[65], TiO_x[66], ZnO[67], etc. To improve even further the reproducibility and performance of the devices, a Poly [(9,9-bis(3'-(N,N-dimethylamino)propyl)-2,7-fluorene)-alt-2,7-(9,9–dioctylfluorene)] (PFN) which is a hole-blocking layer was introduced. The solution processing of the PFN layer is simple, economical and proceeds at room temperature. The introduction of PFN on top of $PCBM_{60}$ would reduce the energetic barrier between the valence band of PCBM and the work function of Al [68]. Furthermore, the PFN layer could act as a capping layer which uniformly covers the underlying perovskite and PCBM. This can result in a limit to possible shunt paths, where the perovskite is not covered by the PCBM and avoid the contact of perovskite and Al electrode. **Table 6** shows the results with the incorporation of a thin (~5nm) PFN layer. This improvement attributed mainly to the better ohmic contact of PCBM and Al, and

the effective hole blocking. **Figure 4-7** shows the EQE curves that were recorded for the samples with PFN and without. A difference of about 7% can be observed in the quantum efficiency in the range of 300-750nm for the sample with PFN. This enhancement is an indication of the improved electrical contact between PCBM and Al.

Table 6

	J_{SC} (mA/cm^2)	V_{OC} (mV)	FF (%)	PCE (%)
	19,0	843	62	10,0
	18,4	880	66	10,7
	18,3	869	65	10,5
	19,3	893	64	11,0
	19,5	891	63	11,0
	19,4	879	67	12,5
Mean value	**19,0**	**875**	**64**	**10,6**

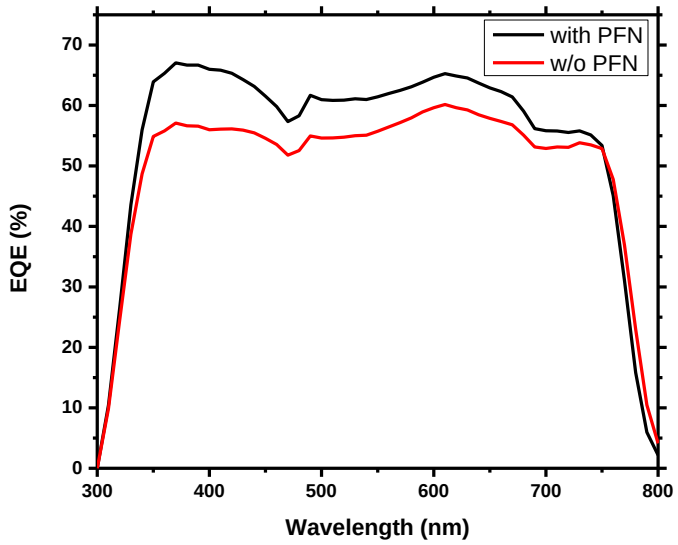

Figure 4-7 EQE spectra of devices without and with PFN interlayer

All the above indicate that a thinner layer of perovskite is desirable at the specific annealing conditions. A better reproducibility was achieved, making a smoother layer as shown in the SEM image. Also, the incorporation of the polyelectrolyte layer of PFN improved the performance of the total device forming a better ohmic contact between the PCBM and Al electrode. The XRD measurements showed that the crystallinity was increased, and no residual precursors were present indicating a more sufficient annealing process. Finally, UV-Vis absorption and photoluminescence spectra confirmed that the perovskite formed had a band gap of 1,6 eV which is in good agreement with the literature [69] [70]. All the factors above had a major role in improving the cell performance.

This optimized device was used as a control device in a project where a modification of ETL was performed. Briefly, an introduction of 5% reduced graphene oxide (rGO) inside the $PCBM_{60}$ layer, improved significantly the Jsc and thus the device performance as shown in **Table 7**. The enhancement in device performance is mainly attributed to enhanced rate of charge carrier extraction as confirmed from photoluminescence spectra in **Figure 4-8 (b)**. Conductivity measurements of PCBM and PCBM:rGO films were performed and it was shown that the conductivity increased from 0,109 mS/cm to 0,495 mS/cm with the incorporation of rGO which is in good agreement with PL and J-V data (**Figure 4-8 (c)**). More details about this project can be found elsewhere [71].

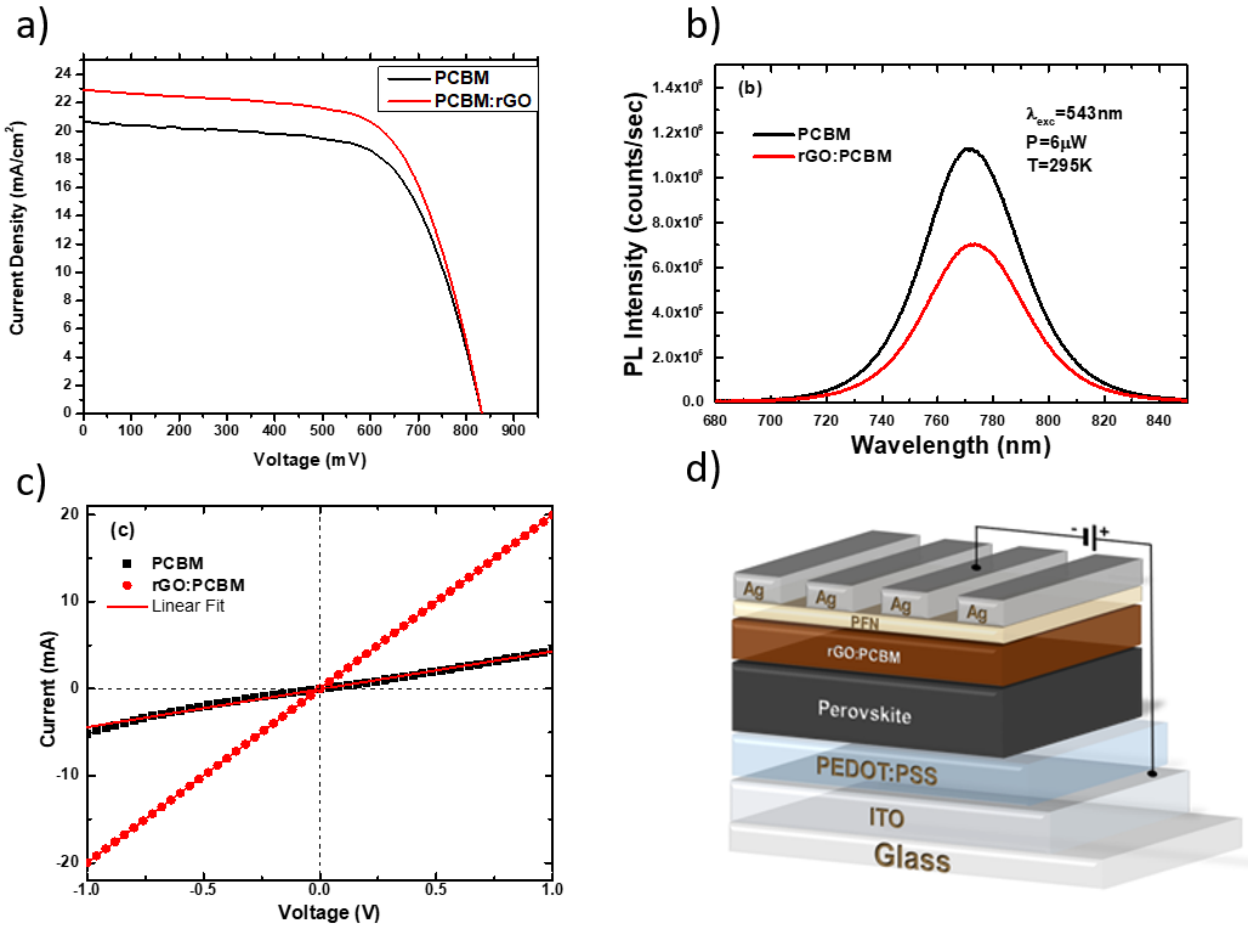

Figure 4-8 (a) J-V curve of pristine and doped PCBM films (b) PL spectra of pristine and doped PCBM film indicating the better charge extraction for the rGO:PCBM (c) Conductivity measurements and (d) device structure

Table 7

rGO Concentration (%)	J_{sc} (mA/cm²)	Voc (mV)	FF (%)	PCE (%) (max.)
0	20,65	836	65,3	11,27 (12,30)
2.5	21,33	844	65,8	11,85 (12,76)
5	22,92	850	65,8	12,82 (13,50)
7.5	22,24	866	64,7	12,46 (13,15)

4.5 Optimization of $MAPbI_3$ perovskite

In general, a lot of studies have shown that non-continuous films were frequently observed when mixing the perovskite precursors in a common solvent (i.e DMF) [1 72 73]. There are many factors that can affect the formation of a pin-hole free perovskite film. The precursor solution blend might interact with the substrate, thus affecting the deposition. Some other factors can be the low viscosity of the solution and the quick crystallization of the as-spun films [74 75]. The performance of such devices is limited, and that limit may arise from a pin-hole film formation of the perovskite. A formation of non-uniform film indicates incomplete substrate coverage and as a result, recombination pathways, high resistance and lose of absorption may occur[76]. To overcome that issue, Xiao et.al reported a new method for depositing a uniform pin-hole free $MAPbI_3$ film. First, PbI_2 and MAI are dissolved into two separate solvents (DMF for PbI_2 and 2-propanol for MAI). By examining the orthogonality and miscibility of these two solvents it can be assumed that DMF and 2-propanol will not interact with each other [77]. Also, PbI_2 has low solubility in 2-propanol so the MAI precursor cannot wash out the PbI_2. The PbI_2 solution is then casted on the HTL-covered substrate and thermally annealed. After that, MAI solution is spin-coated on the PbI_2 film which quickly reacts with the underlaying layer and is thermally annealed. The reaction can be evidenced by an immediate color change of the film. During the annealing process, the MAI and PbI_2 layers interact with each other forming the $MAPbI_3$ film. The specific method described above is called the interdiffusion method.

To prepare a $MAPbI_3$ perovskite by the interdiffusion method, the process reported by Xiao et.al was followed. Two separate solutions were made dissolving 450 mg of PbI_2 and 45 mg of MAI in DMF and 2-propanol respectively. At the first attempt, the perovskite could not be formed as a yellow film was formed, an indication of a non-perovskite film formation. This result was coming from the fact that PbI_2 cannot be fully dissolved in DMF and a milky solution was obtained. The supersaturated PbI_2 solution required heating for several hours to give a clear yellow solution (**Figure 4-9**). To achieve better solubility the same procedure was applied for the MAI solution. The device optimization was first started at different revolution per minutes (rpm) for both PbI_2 and MAI layers and their combinations. In this case PEDOT:PSS was chosen as the HTL. A careful optimization of deposition conditions resulted in a PCE of 12,9% as it can be seen in **table 8** and **Figure 4-10**.

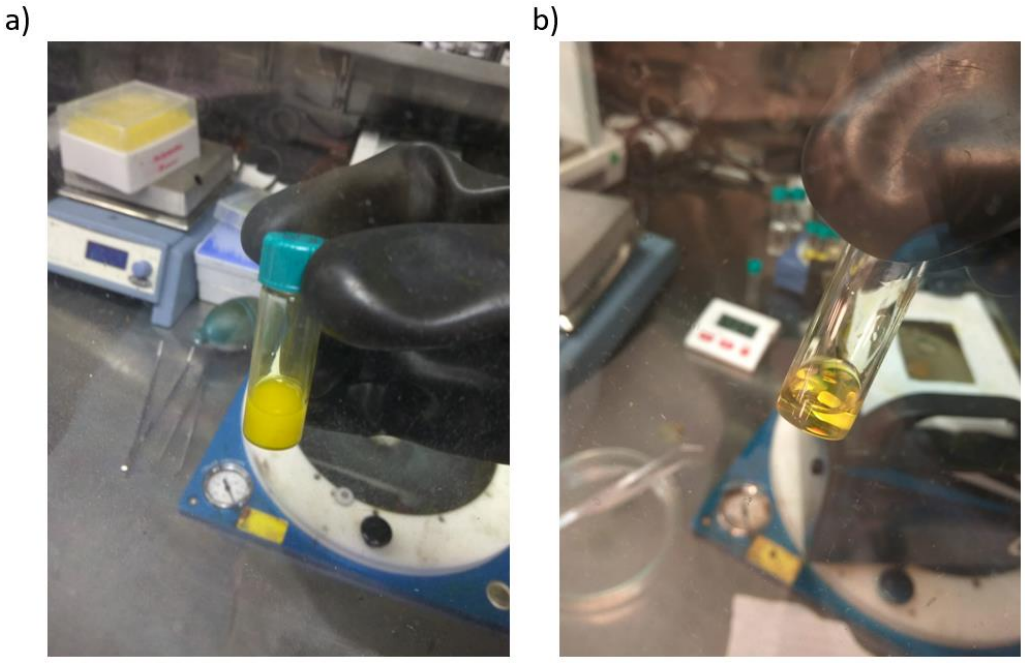

Figure 4-9 The PbI_2 dissolved in DMF without any heating resulted in a milky solution (left). When heated at 70°C overnight, a clear yellow solution of PbI_2 was obtained (right).

Table 8

PbI_2 rpm	MAI rpm	Jsc (mA/cm2)	Voc (mV)	FF	PCE %
4000	4000	12,8	800	60	6,1
4000	5000	14,8	798	62	7,3
4000	6000	13,2	730	62	6,0
5000	4000	15,5	840	63	8,2
5000	5000	17,4	800	65	9,0
5000	6000	17,8	920	64	10,4
6000	4000	19,3	910	61	10,8
6000	5000	20,0	922	65	12,0
6000	**6000**	**21,7**	**926**	**64**	**12,9**

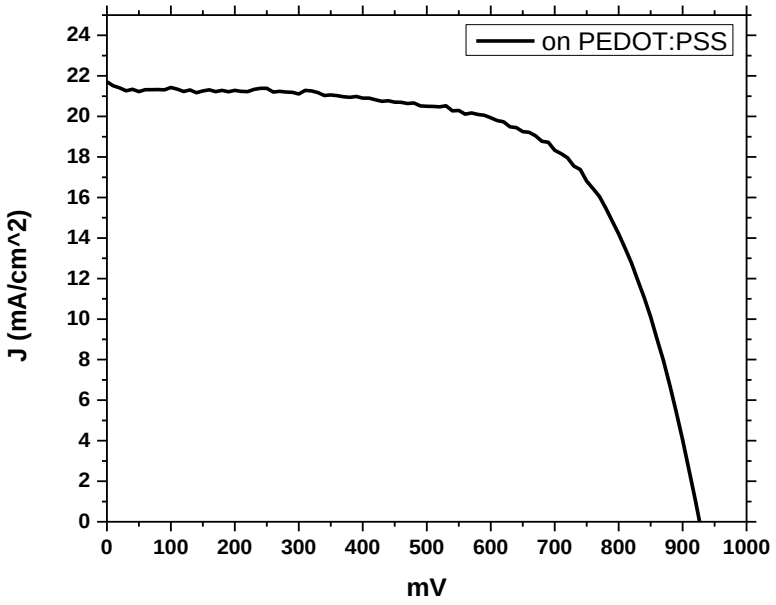

Figure 4-10 The characteristic J-V curve of the optimized device.

Such a result was still low for planar inverted structure so different ETL and HTL should be examined. The low efficiency could be attributed to the low work function of PEDOT:PSS which limits the Voc of the device to about 900mV [78] and also due to the non-uniform layer of perovskite.

4.6 Introduction of PTAA

Different polymers have been used for hole transporting layers such as poly [N, N0-bis(4-butylphenyl)-N, N0-bis (phenyl)benzidine] (poly-TPD)[79] which resulted in a V_{oc} value of 1 V because of a better CB and VB alignment and a better crystallization of the perovskite. Furthermore, through the plethora of HTL materials, a careful selection must be done in terms of solvent orthogonality. For example, the hole transporting layer should not be affected by the solvent of the perovskite precursor which in this case is DMF. For this case Poly[bis(4-phenyl) (2,4,6-trimethylphenyl) amine Poly(triarylamine) PTAA was used as the HTL which is sustainable to DMF wash. Compared to PEDOT:PSS, the valence band of PTAA is -5.25 eV which is closer to the VB of the perovskite, while the valence band of PEDOT:PSS is -5.1 eV indicating that PTAA is more favorable HTL for $MAPbI_3$ absorber (**Figure 4-11**).

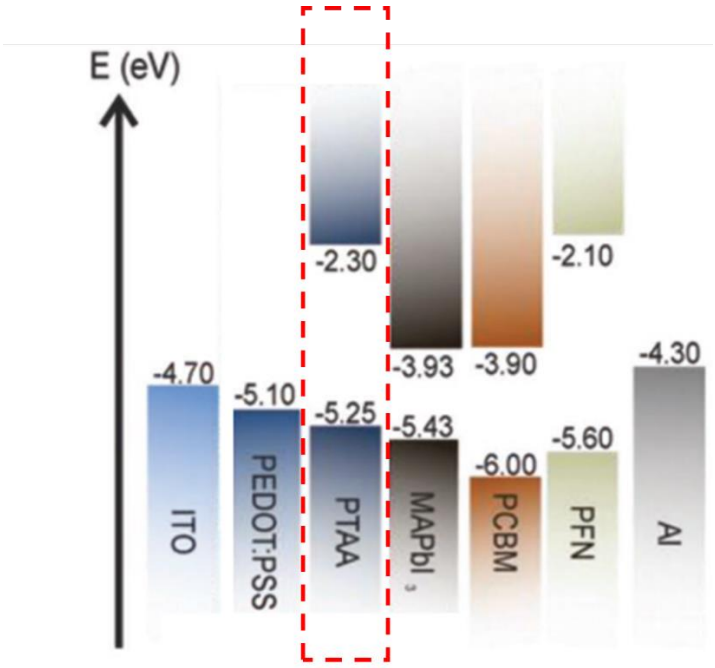

Figure 4-11 Energy diagram of PEDOT:PSS and PTAA compared to the $MAPbI_3$ absorber

By replacing PEDOT:PSS with PTAA, an optimization for the thickness of the new HTL was carried out. Different concentration of PTAA solution were tested at different rounds per minute (rpm). In **table 9** it is shown that the optimum concentration was found to be 10 mg/ml which resulted in a PCE close to 13%. Significant improvement in terms of Voc is observed as expected. The estimated thickness for that concentration is about 50nm. **Figure 4-12** shows the J-V curves of the devices with different PTAA concentration.

Table 9

PTAA concentration (mg/ml)	Jsc (mA/cm^2)	Voc (mV)	FF	PCE (%)
4	6,3	827	56	3,5
8	14,3	894	65	9,9
10	**18,5**	**994**	**70**	**13,0**
12	17,8	978	70	12,3
15	15,6	904	61	10,2

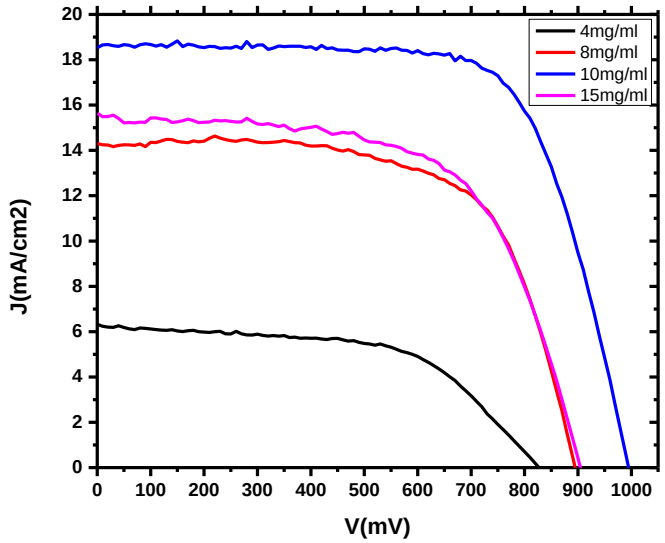

Figure 4-12 J-V curves of different PTAA thickness

4.7 Doping of PTAA

Even though PTAA has more favorable energy levels for the $MAPbI_3$ absorber, its conductivity is quiet low [80]. Thus, to increase conductivity, the PTAA was doped with a small molecule (2,3,5,6-Tetrafluoro-2,5-cyclohexadiene-1,4-diylidene) dimalononitrile (F4-TCNQ). By making the PTAA more conductive, an improvement of FF was achieved at an optimum doping concentration of 1.5% wt as show in **table 10** and **Figure 4-13**.

Table 10

F4-TCNQ wt% ratio	Jsc (mA/cm^2)	Voc (mV)	FF	PCE (%)
0	18,5	994	70	13,0
0,5	19,3	981	77	14,5
1	19,7	990	77	15,0
1,5	**20,1**	**1014**	**76**	**15,5**
2	20,0	989	70	13,8

The optimum doping concentration was found to be 1,5 wt% and resulted in a PCE value of 15,5%. Further increasing the concentration of the F4-TCNQ decreased the efficiency possibly due to the formation of aggregates of that small molecule [viii].

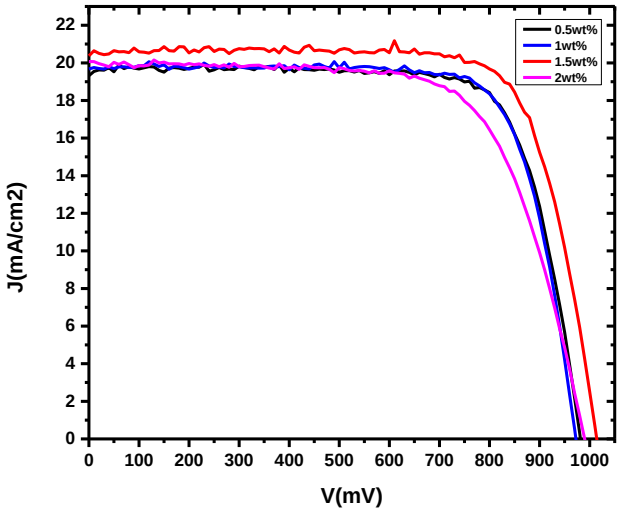

Figure 4-13 shows the JV curves of the doping optimization.

To investigate the crystallinity of $MAPbI_3$, XRD measurements were performed on both PTAA and PEDOT:PSS covered substrates **Figure 4-14**. The two dominant peaks for both cases at 14° and 28,4° correspond to the (110) and (220) lattice planes of the tetragonal perovskite phase respectively [81]. The weaker peaks at 24,4° and 31,8° are attributed to the (202) and (310) reflections respectively. To compare the crystallinity of the perovskite deposited on the two different HTL substrates, full width at half maximum (FWHM) was calculated for the (110) peak. For the case where perovskite was grown on PEDOT:PSS, the FWHM was found to be 0,169° whereas when PTAA was used the FWHM was reduced to 0,125°. This reduction in the value of FWHM for the case of PTAA indicates increased crystallinity and larger grains of perovskite [82].

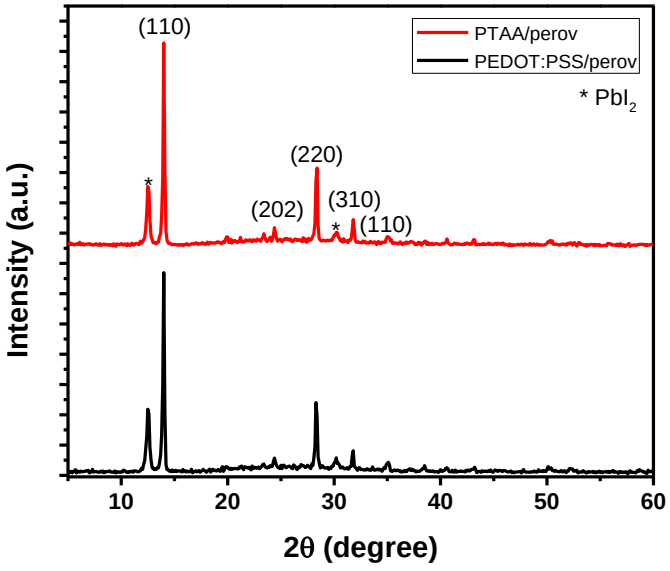

Figure 4-14 XRD patterns of $MAPbI_3$ on PTAA and PEDOT:PSS

However, in both cases, the peak at 12,7° is present which corresponds to PbI_2. That peak originates from the unreacted PbI_2 content which is present in the final film. The presence of PbI_2 is a common thing when using the two-step deposition method[83, 84]. Some studies have concluded that the presence of small amount of PbI_2 in the perovskite film is beneficial for device performance [85]. PbI_2 could passivate the grain boundaries resulting in a reduction of recombination and enhancing the stability and performance [86]. Some other studies suggest that PbI_2 may passivate the TiO_2 interface decreasing the hole recombination and at the same time matching the band edge of TiO_2 and perovskite. As for the HTL and perovskite

interface, PbI_2 could act as an electron blocking layer, facilitating hole injection and thus reducing the recombination. However, if the presence of PbI_2 is too big and a thick layer is formed, an energetic barrier is formed which prevents the charge transfer[87].

To further support the conclusion from XRD measurements, SEM and AFM images were taken to investigate the quality and morphology of the perovskite film. **Figure 4-15** shows SEM images of perovskite deposited on both PEDOT:PSS and PTAA covered substrates. It is clearly seen that smoother and more compact film of perovskite is formed on the PTAA. Larger grains of perovskite would have reduced trap states and fewer grain boundaries, thus enhancing charge extraction and V_{oc} (8). The average grain size of perovskite deposited on PTAA is about 400nm where for the PEDOT:PSS the average grain size is about 270nm. Bigger grains of perovskite are desirable to reduce the grain boundaries where a large density of traps is present causing charge recombination[88]. This finding is in good agreement with XRD data, which indicates that the better crystallinity of perovskite is attributed to the bigger grains and more compact film.

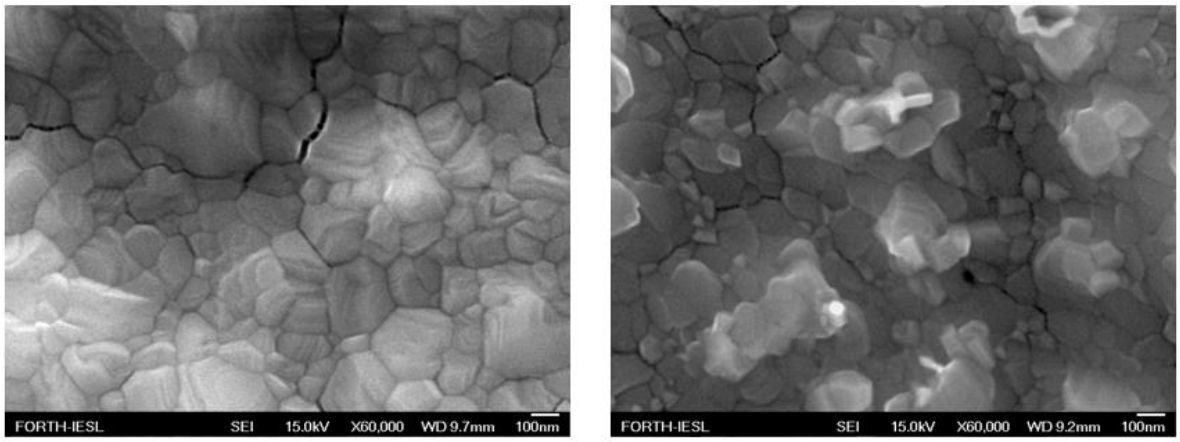

Figure 4-15 SEM images of MAPbI3 film on PTAA (left) and PEDOT:PSS (right).

To study morphology and the interface of the perovskite and HTL, AFM images were taken. **Figure 4-16 (a) and (b)** shows the morphology of PEDOT:PSS and PTAA. The average roughness value of PEDOT:PSS and PTAA was 0,942 nm and 0,580 nm respectively. **Figure 4-16 (c)** and **(d)** show the perovskite deposited on PEDOT:PSS and PTAA respectively. The average value of perovskite deposited on PEDOT:PSS and PTAA was 41,447 nm and 34,001 nm. It is apparent that a smoother layer of perovskite is formed on top of PTAA thus forming bigger grains and pin-hole free film.

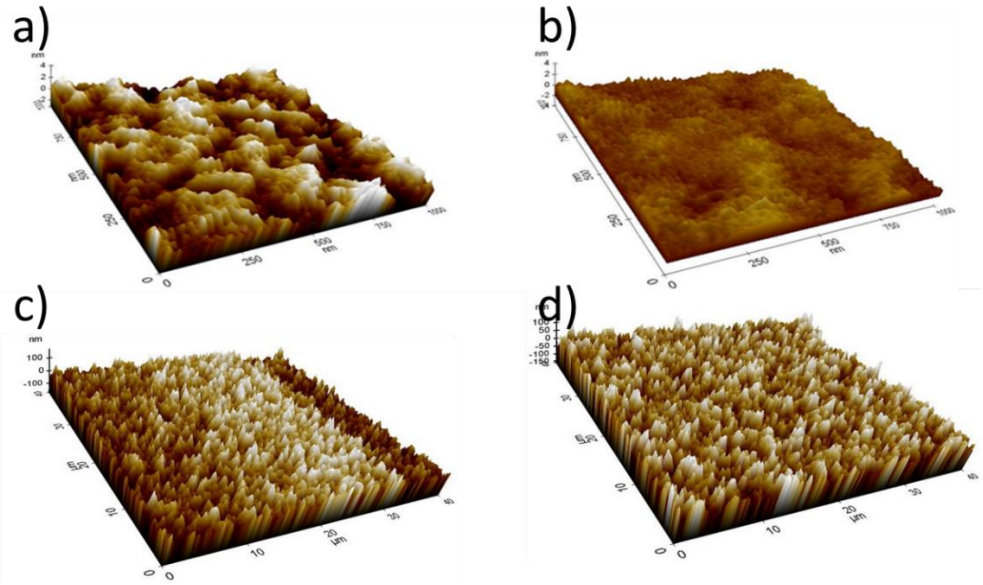

Figure 4-16 AFM images of PEDOT:PSS (a) and PTAA (b) and perovskite deposited on PEDOT:PSS (c) and PTAA (d).

To investigate the charge extraction properties of both PTAA and PEDOT:PSS, steady-state photoluminescence spectra were measured. The sample configuration was glass/HTL/perovskite. **Figure 4-17** shows the photoluminescence spectra of PEDOT:PSS/perovskite and PTAA/perovskite. It is evident that when PTAA is used as an HTL, significant quenching is observed compared to the PEDOT:PSS, an indication that PTAA has a better rate of charge extraction [24]. That finding is in good agreement with the J-V and EQE data, suggesting that replacing PEDOT:PSS with PTAA enhances device performance.

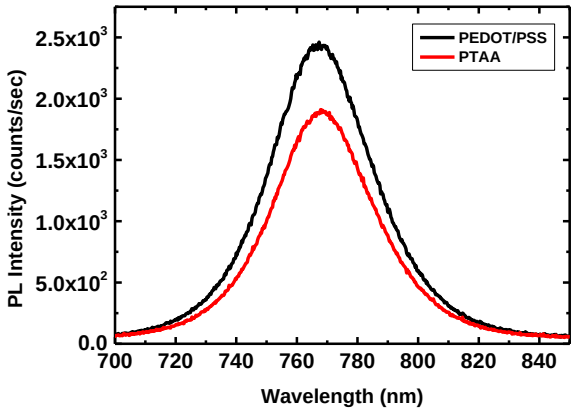

Figure 4-17 Photoluminescence spectra of perovskite deposited on PTAA and PEDOT:PSS. The quenching of PL signal is an indication of a better charge carrier extraction for the case of PTAA

The EQE spectrum is show in **Figure 4-18 (a)** for both cases. Below 450 nm the PTAA based device showed a response which is attributed to the low transmission of light [89]. For the PTAA, a slight and uniform increase is observed between 450 nm to 800 nm. This slight enhancement could be attributed to the better film quality as shown in SEM images and XRD patterns and better conductivity. **Figure 4-18 (b)** shows the J-V curves of both cases. It is clear that the enhancement in the device performance is due to the improved Voc.

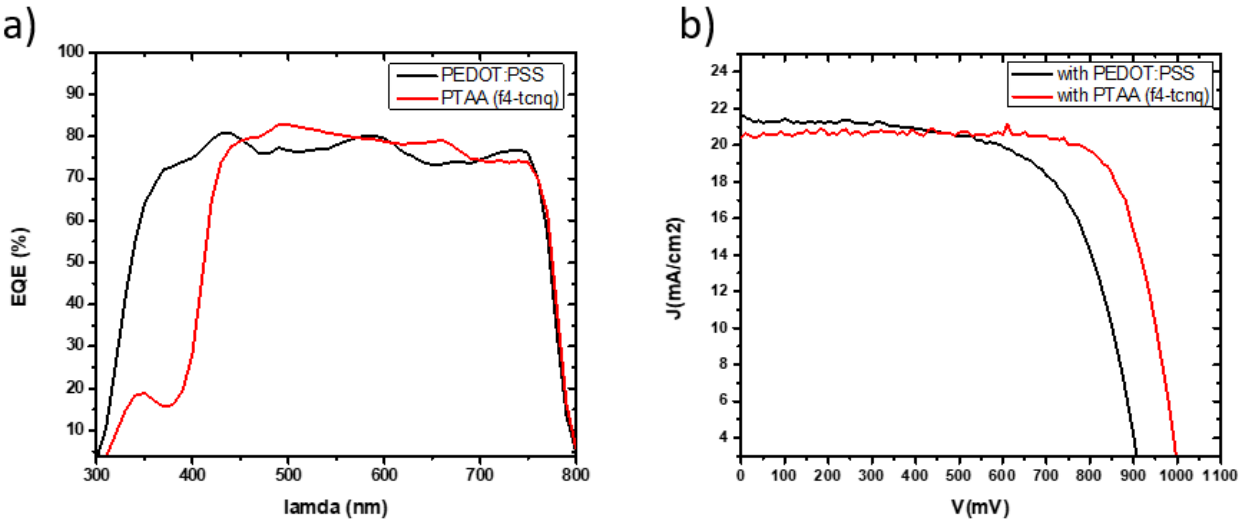

Figure 4-18 EQE spectra of PTAA and PEDOT:PSS based devices (a). J-V curves of those devices (b).

Photoluminescence and UV-vis absorption spectra are shown in **figure 4-19** confirming the formation of $MAPbI_3$ perovskite with a band gap of 1,59 eV which is in good agreement with the literature.

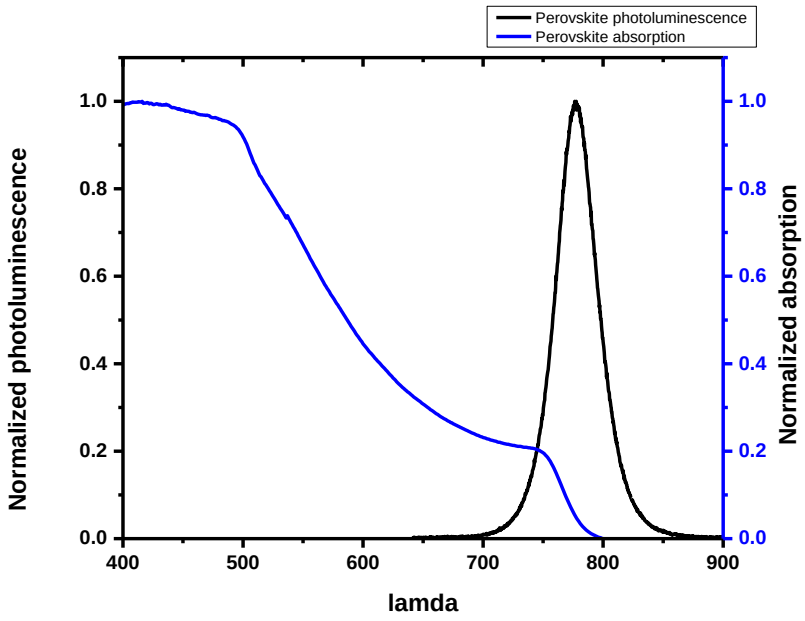

Figure 4-19 UV-vis and PL spectra of the $MAPbI_3$ perovskite

In conclusion, $MAPbI_3$ perovskite was optimized first on PEDOT:PSS hole-transporting material resulting in a PCE of 13%. As shown in previous study, the thickness of perovskite is crucial in terms of device performance thus an optimum thickness should be found. A PCE of 13% was quiet low for planar inverted architecture, so for this case a different HTL was used. As shown above, PTAA is more compatible HTL for $MAPbI_3$ absorber due to the lower offset of VBM between each other. The extraction of carriers is more efficient due to the better CB and VB alignment and more crystalline perovskite film. Finally, after careful doping optimization of PTAA with a small molecule, a PCE of 15,5% was achieved.

This optimized device based on doped PTAA and $MAPbI_3$ was used in another project where the stability of such devices was studied. Briefly, an introduction of solution-processed MoS_2 flakes between the PTAA and $MAPbI_3$ took place enhancing slightly the device performance with a PCE of about 17%. The improved device performance is attributed to the reduced energetic offset between PTAA and $MAPbI_3$ as shown in figure. However, more importantly MoS_2-based interlayer device achieved T_{80} lifetime of 568 hours which was state of the art stability for planar inverted PeSCs. Such stability was achieved due to the fact that MoS_2 flakes prevented the diffusion of water molecules from the ITO and doped-PTAA hygroscopic layer (**Figure 4-20)**. More details can be found elsewhere [90].

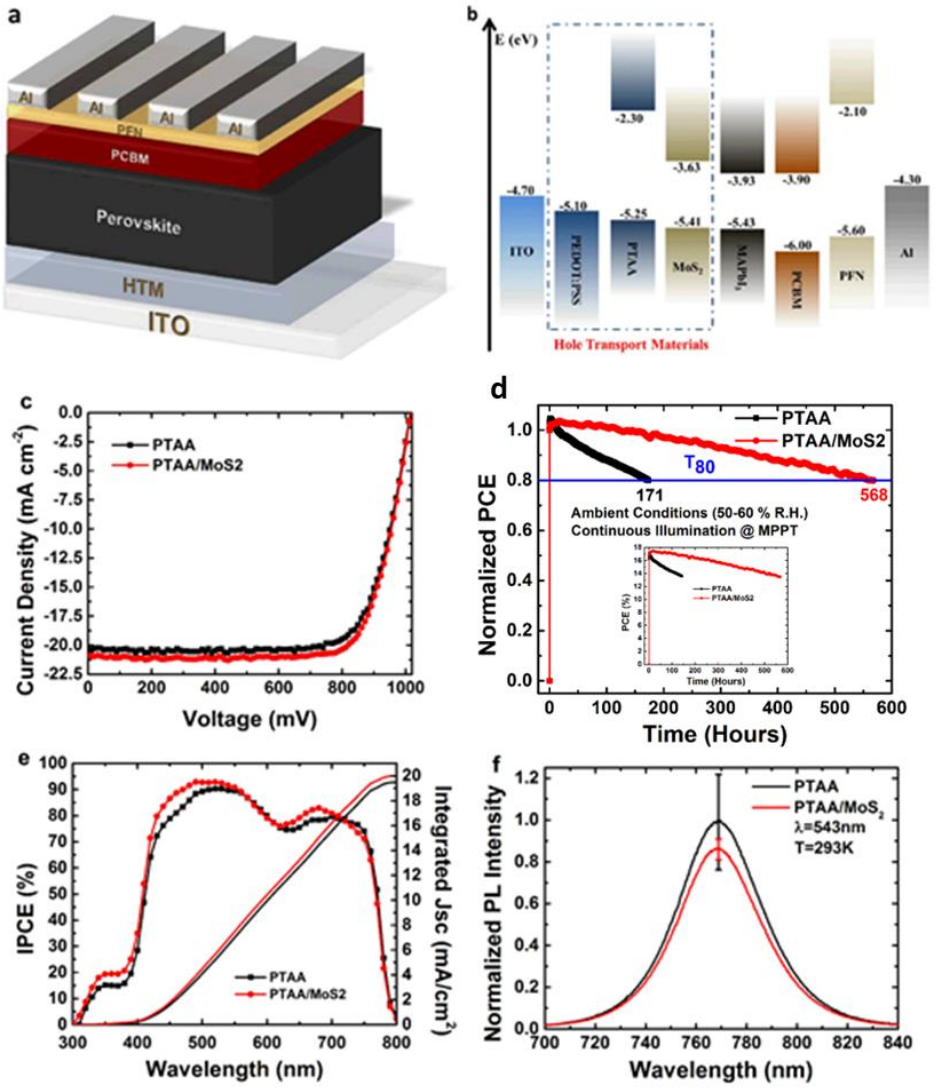

Figure 4-20 (a) device structure (b) Energy levels of the constructed device where MoS_2 is shown to have suitable energy levels for better charge extraction (c) J-V curves with and without MoS_2 interlayer (d) Device stability for T_{80} (e) and (f) EQE and PL spectra

5. Conclusion

In conclusion, two hybrid perovskites were optimized and characterized. For the mixed halide perovskite, a critical point was found to be the thickness and annealing time of the active layer. A thinner layer resulted in fewer pinholes and more compact film as shown from SEM images. Moreover, such a film was fully crystalline with no residual precursors which improved the reproducibility of the devices. Furthermore, an introduction of an interlayer (PFN) took place which resulted in a PCE of about 11% due to the better ohmic contact between PCBM and Al. For the methylammonium lead triiodide perovskite, an optimization of thickness was introduced but the device performance was still low. A different HTL was used with better energy levels which resulted in a gain of about 100mV in Voc. Doping the new HTL resulted a PCE of about 15,5%. By comparing the two different HTLs, it was found that the enhancement in device performance was attributed to a better interface between the PTAA and perovskite and better charge extraction.

References

[1] Kojima, A., Teshima, K., Shirai, Y. and Miyasaka, T. (2009). Organometal Halide Perovskites as Visible-Light Sensitizers for Photovoltaic Cells. *Journal of the American Chemical Society*, 131(17), pp.6050-6051.

[2] Available at http://www.nrel.gov/ncpv/images/efficiency_chart.jpg

[3] Available at http://www.worldometers.info/world-population/#table-forecast

[4] Available at http://www.eia.gov

[5] Available at https://en.wikipedia.org/wiki/Solar_irradiance

[6] Chart available at: http://www.nrel.gov/ncpv/images/efficiency_chart.jpg

[7] Dubey, A., Adhikari, N., Mabrouk, S., Wu, F., Chen, K., Yang, S. and Qiao, Q. (2018). A strategic review on processing routes towards highly efficient perovskite solar cells. *Journal of Materials Chemistry A*, 6(6), pp.2406-2431.

[8] Wikipedia available at: https://en.wikipedia.org/wiki/Perovskite

[9] Schlom, D., Chen, L., Pan, X., Schmehl, A. and Zurbuchen, M. (2008). A Thin Film Approach to Engineering Functionality into Oxides. Journal of the American Ceramic Society, 91(8), pp.2429-2454.

[10] Shi, S., Li, Y., Li, X. and Wang, H. (2015). Advancements in all-solid-state hybrid solar cells based on organometal halide perovskites. *Materials Horizons*, 2(4), pp.378-405.

[11]Kim, H., Lee, C., Im, J., Lee, K., Moehl, T., Marchioro, A., Moon, S., Humphry-Baker, R., Yum, J., Moser, J., Grätzel, M. and Park, N. (2012). Lead Iodide Perovskite Sensitized All-Solid-State Submicron Thin Film Mesoscopic Solar Cell with Efficiency Exceeding 9%. *Scientific Reports*, 2(1).

[12] Available at: http://www.slideshare.net/aceronur/perovskite-temelli-gne-hcreleri

[13] Sum, T. and Mathews, N. (2014). Advancements in perovskite solar cells: photophysics behind the photovoltaics. *Energy Environ. Sci*., 7(8), pp.2518-2534.

[14] Vaenas, N., Konios, D., Stergiopoulos, T. and Kymakis, E. (2015). Slow photocharging and reduced hysteresis in low-temperature processed planar perovskite solar cells. *RSC Advances*, 5(130), pp.107771-107776.

[15] Available at: http://pveducation.org/

[16] Available at: https://en.wikipedia.org/wiki/Valence_and_conduction_bands

[17] Gao, P., Grätzel, M. and Nazeeruddin, M. (2014). Organohalide lead perovskites for photovoltaic applications. *Energy Environ. Sci*., 7(8), pp.2448-2463.

[18] Edri, E., Kirmayer, S., Mukhopadhyay, S., Gartsman, K., Hodes, G. and Cahen, D. (2014). Elucidating the charge carrier separation and working mechanism of CH3NH3PbI3−xCl x perovskite solar cells. *Nature Communications*, 5(1).

[19] Brittman, S., Adhyaksa, G. and Garnett, E. (2015). The expanding world of hybrid perovskites: materials properties and emerging applications. *MRS Communications*, 5(01), pp.7-26.

[20] Cui, J., Yuan, H., Li, J., Xu, X., Shen, Y., Lin, H. and Wang, M. (2015). Recent progress in efficient hybrid lead halide perovskite solar cells. *Science and Technology of Advanced Materials*, 16(3), p.036004.

[21] Burschka, J., Pellet, N., Moon, S., Humphry-Baker, R., Gao, P., Nazeeruddin, M. and Grätzel, M. (2013). Sequential deposition as a route to high-performance perovskite-sensitized solar cells. *Nature*, 499(7458), pp.316-319.

[22] Hsiao, Y., Wu, T., Li, M., Liu, Q., Qin, W. and Hu, B. (2015). Fundamental physics behind high-efficiency organo-metal halide perovskite solar cells. *Journal of Materials Chemistry A*, 3(30), pp.15372-15385.

[23] Grancini, G., Marras, S., Prato, M., Giannini, C., Quarti, C., De Angelis, F., De Bastiani, M., Eperon, G., Snaith, H., Manna, L. and Petrozza, A. (2014). The Impact of the Crystallization Processes on the Structural and Optical Properties of Hybrid Perovskite Films for Photovoltaics. *The Journal of Physical Chemistry Letters*, 5(21), pp.3836-3842.

[24] Stranks, S., Eperon, G., Grancini, G., Menelaou, C., Alcocer, M., Leijtens, T., Herz, L., Petrozza, A. and Snaith, H. (2013). Electron-Hole Diffusion Lengths Exceeding 1 Micrometer in an Organometal Trihalide Perovskite Absorber. *Science*, 342(6156), pp.341-344.

[25] Xing, G., Mathews, N., Sun, S., Lim, S., Lam, Y., Gratzel, M., Mhaisalkar, S. and Sum, T. (2013). Long-Range Balanced Electron- and Hole-Transport Lengths in Organic-Inorganic CH3NH3PbI3. *Science*, 342(6156), pp.344-347.

[26] Travis, W., Glover, E., Bronstein, H., Scanlon, D. and Palgrave, R. (2016). On the application of the tolerance factor to inorganic and hybrid halide perovskites: a revised system. *Chemical Science*, 7(7), pp.4548-4556.

[27] Han, G., Hadi, H., Bruno, A., Kulkarni, S., Koh, T., Wong, L., Soci, C., Mathews, N., Zhang, S. and Mhaisalkar, S. (2018). Additive Selection Strategy for High Performance Perovskite Photovoltaics. *The Journal of Physical Chemistry C,* 122(25), pp.13884-13893.

[28] Shen, K., Hu, J., Liang, Z., Hu, J., Sun, H., Jiang, Z. and Song, F. (2018). Emerging Characterizing Techniques in the Fine Structure Observation of Metal Halide Perovskite Crystal. *Crystals*, 8(6), p.232.

[29] Available at: https://en.wikipedia.org/wiki/Air_mass_(solar_energy)

[30] Green, M., Ho-Baillie, A. and Snaith, H. (2014). The emergence of perovskite solar cells. *Nature* Photonics, 8(7), pp.506-514.

[31] Available at https://en.wikipedia.org/wiki/Shockley%E2%80%93Queisser_limit

[32] McMeekin, D., Sadoughi, G., Rehman, W., Eperon, G., Saliba, M., Horantner, M., Haghighirad, A., Sakai, N., Korte, L., Rech, B., Johnston, M., Herz, L. and Snaith, H. (2016). A mixed-cation lead mixed-halide perovskite absorber for tandem solar cells. *Science*, 351(6269), pp.151-155.

[33] Ye, M., He, C., Iocozzia, J., Liu, X., Cui, X., Meng, X., Rager, M., Hong, X., Liu, X. and Lin, Z. (2017). Recent advances in interfacial engineering of perovskite solar cells. *Journal of Physics D: Applied Physics*, 50(37), p.373002.

[34] Eperon, G., Stranks, S., Menelaou, C., Johnston, M., Herz, L. and Snaith, H. (2014). Formamidinium lead trihalide: a broadly tunable perovskite for efficient planar heterojunction solar cells. *Energy & Environmental Science*, 7(3), p.982.

[35] Li, Y., Yan, W., Li, Y., Wang, S., Wang, W., Bian, Z., Xiao, L. and Gong, Q. (2015). Direct Observation of Long Electron-Hole Diffusion Distance in CH3NH3PbI3 Perovskite Thin Film. Scientific Reports, 5(1).

[36] Snaith, H., Abate, A., Ball, J., Eperon, G., Leijtens, T., Noel, N., Stranks, S., Wang, J., Wojciechowski, K. and Zhang, W. (2014). Anomalous Hysteresis in Perovskite Solar Cells. *The Journal of Physical Chemistry Letters*, 5(9), pp.1511-1515.

[37] Song, T., Chen, Q., Zhou, H., Jiang, C., Wang, H., (Michael) Yang, Y., Liu, Y., You, J. and Yang, Y. (2015). Perovskite solar cells: film formation and properties. *Journal of Materials Chemistry A*, 3(17), pp.9032-9050.

[38] Wang, Z., Li, M., Yuan, D., Shi, X., Ma, H. and Liao, L. (2015). Improved Hole Interfacial Layer for Planar Perovskite Solar Cells with Efficiency Exceeding 15%. *ACS Applied Materials & Interfaces*, 7(18), pp.9645-9651.

[39] Available at https://en.wikipedia.org/wiki/Ultrasonic_cleaning

[40] Available at http://www.mbraun.com/products/encapsulation-equipment/uv-cleaning/mb-uv-o3-cleaner

[41] Available at https://en.wikipedia.org/wiki/Spin_coating

[42] Available at http://www.ossila.com/pages/spin-coating

[43] Available at https://en.wikipedia.org/wiki/Glovebox

[44] Available at http://www.semicore.com/news/71-thin-film-deposition-thermal-evaporation

[45] Available at http://www.hindawi.com/journals/ijp/2014/198734/fig6/

[46] Available at http://plasticphotovoltaics.org/lc/characterization/lc-advanced-c/lc-uvvis.html

[47] Πατεράκης Σ. Γεώργιος "Φωτοβολταϊκές Διατάξεις και συσκευές με χρήση πολυμερικών υλικών και στρώσεων γραφενίου" Master's thesis, University of Patras 2015

[48] Available at http://plasticphotovoltaics.org/lc/characterization/lc-advanced-c/lc-xray.html

[49] Available at http://ssp.physics.upatras.gr/X-Ray%20Diffraction.html

[50] Available at https://en.wikipedia.org/wiki/Solar_simulator

[51] Available at http://www.nist.gov/pml/div686/solar-simulator.cfm

[52] Available at https://en.wikipedia.org/wiki/Scanning_electron_microscope

[53] Available at https://en.wikipedia.org/wiki/Quantum_efficiency

[54] Available at https://en.wikipedia.org/wiki/Atomic_force_microscopy

[55] Tidhar, Y., Edri, E., Weissman, H., Zohar, D., Hodes, G., Cahen, D., Rybtchinski, B. and Kirmayer, S. (2014). Crystallization of Methyl Ammonium Lead Halide Perovskites: Implications for Photovoltaic Applications. *Journal of the American Chemical Society*, 136(38), pp.13249-13256.

[56] Samiee, M., Konduri, S., Ganapathy, B., Kottokkaran, R., Abbas, H., Kitahara, A., Joshi, P., Zhang, L., Noack, M. and Dalal, V. (2014). Defect density and dielectric constant in perovskite solar cells. *Applied Physics Letters*, 105(15), p.153502.

[57] Du, P., Hu, X., Yi, C., Liu, H., Liu, P., Zhang, H. and Gong, X. (2015). Self-Powered Electronics by Integration of Flexible Solid-State Graphene-Based Supercapacitors with High Performance Perovskite Hybrid Solar Cells. *Advanced Functional Materials*, 25(16), pp.2420-2427.

[58] Yang, Z., Chueh, C., Zuo, F., Kim, J., Liang, P. and Jen, A. (2015). High-Performance Fully Printable Perovskite Solar Cells via Blade-Coating Technique under the Ambient Condition. *Advanced Energy Materials*, 5(13), p.1500328.

[59] Wang, W., Yuan, J., Shi, G., Zhu, X., Shi, S., Liu, Z., Han, L., Wang, H. and Ma, W. (2015). Inverted Planar Heterojunction Perovskite Solar Cells Employing Polymer as the Electron Conductor. *ACS Applied Materials & Interfaces*, 7(7), pp.3994-3999.

[60] Xu, M., Zhang, H., Zhang, S., Zhu, H., Su, H., Liu, J., Wong, K., Liao, L. and Choy, W. (2015). A low temperature gradual annealing scheme for achieving high performance perovskite solar cells with no hysteresis. *Journal of Materials Chemistry A*, 3(27), pp.14424-14430.

[61] Vaenas, N., Konios, D., Stergiopoulos, T. and Kymakis, E. (2015). Slow photocharging and reduced hysteresis in low-temperature processed planar perovskite solar cells. *RSC Advances*, 5(130), pp.107771-107776.

[62] Zhang, W., Saliba, M., Moore, D., Pathak, S., Hörantner, M., Stergiopoulos, T., Stranks, S., Eperon, G., Alexander-Webber, J., Abate, A., Sadhanala, A., Yao, S., Chen, Y., Friend, R., Estroff, L., Wiesner, U. and Snaith, H. (2015). Ultrasmooth organic–inorganic perovskite thin-film formation and crystallization for efficient planar heterojunction solar cells. *Nature Communications*, 6(1)

[63] Wang, M., Shi, C., Zhang, J., Wu, N. and Ying, C. (2015). Influence of PbCl2 content in PbI2 solution of DMF on the absorption, crystal phase, morphology of lead halide thin films and photovoltaic performance in planar perovskite solar cells. *Journal of Solid State Chemistry*, 231, pp.20-24.

[64] Chiang, C., Tseng, Z. and Wu, C. (2014). Planar heterojunction perovskite/PC71BM solar cells with enhanced open-circuit voltage via a (2/1)-step spin-coating process. *J. Mater. Chem. A*, 2(38), pp.15897-15903.

[65] Seo, J., Park, S., Chan Kim, Y., Jeon, N., Noh, J., Yoon, S. and Seok, S. (2014). Benefits of very thin PCBM and LiF layers for solution-processed p–i–n perovskite solar cells. *Energy Environ. Sci.*, 7(8), pp.2642-2646.

[66] Docampo, P., Ball, J., Darwich, M., Eperon, G. and Snaith, H. (2013). Efficient organometal trihalide perovskite planar-heterojunction solar cells on flexible polymer substrates. *Nature Communications*, 4(1)

[67] Guo, F., Azimi, H., Hou, Y., Przybilla, T., Hu, M., Bronnbauer, C., Langner, S., Spiecker, E., Forberich, K. and Brabec, C. (2015). High-performance semitransparent perovskite solar cells with solution-processed silver nanowires as top electrodes. *Nanoscale*, 7(5), pp.1642-1649.

[68] Hong, S., Lee, J., Kang, H., Kim, G., Kee, S., Lee, J., Jung, S., Park, B., Kim, S., Back, H., Yu, K. and Lee, K. (2018). High-efficiency large-area perovskite photovoltaic modules achieved via electrochemically assembled metal-filamentary nanoelectrodes. *Science Advances*, 4(8), p.eaat3604.

[69] Huang, J., Wang, M., Ding, L., Deng, J. and Yao, X. (2015). Efficiency enhancement of the MAPbI3−xClx-based perovskite solar cell by a two-step annealing procedure. *Semiconductor Science and Technology*, 31(2), p.025009.

[70] Zhang, W., Saliba, M., Moore, D., Pathak, S., Hörantner, M., Stergiopoulos, T., Stranks, S., Eperon, G., Alexander-Webber, J., Abate, A., Sadhanala, A., Yao, S., Chen, Y., Friend, R., Estroff, L., Wiesner, U. and Snaith, H. (2015). Ultrasmooth organic–inorganic perovskite thin-film formation and crystallization for efficient planar heterojunction solar cells. *Nature Communications*, 6(1).

[71] Kakavelakis, G., Maksudov, T., Konios, D., Paradisanos, I., Kioseoglou, G., Stratakis, E. and Kymakis, E. (2016). Efficient and Highly Air Stable Planar Inverted Perovskite Solar Cells with Reduced Graphene Oxide Doped PCBM Electron Transporting Layer. *Advanced Energy Materials*, 7(7), p.1602120.

[72] Hodes, G. (2013). Perovskite-Based Solar Cells. *Science*, 342(6156), pp.317-318.

[73] Docampo, P., Ball, J., Darwich, M., Eperon, G. and Snaith, H. (2013). Efficient organometal trihalide perovskite planar-heterojunction solar cells on flexible polymer substrates. *Nature Communications*, 4(1).

[74] Wang, Q., Shao, Y., Dong, Q., Xiao, Z., Yuan, Y. and Huang, J. (2014). Large fill-factor bilayer iodine perovskite solar cells fabricated by a low-temperature solution-process. *Energy Environ. Sci*., 7(7), pp.2359-2365.

[75] Xiao, Z., Bi, C., Shao, Y., Dong, Q., Wang, Q., Yuan, Y., Wang, C., Gao, Y. and Huang, J. (2014). Efficient, high yield perovskite photovoltaic devices grown by interdiffusion of solution-processed precursor stacking layers. *Energy Environ. Sci*., 7(8), pp.2619-2623.

[76] Eperon, G., Burlakov, V., Docampo, P., Goriely, A. and Snaith, H. (2013). Morphological Control for High Performance, Solution-Processed Planar Heterojunction Perovskite Solar Cells. *Advanced Functional Materials*, 24(1), pp.151-157

[77] Available at https://www.csustan.edu/sites/default/files/groups/Chemistry/Drake/documents/solvent_miscibility_table.pdf

[78] Wang, Q., Bi, C. and Huang, J. (2015). Doped hole transport layer for efficiency enhancement in planar heterojunction organolead trihalide perovskite solar cells. *Nano Energy*, 15, pp.275-280.

[79] Zhao, D., Sexton, M., Park, H., Baure, G., Nino, J. and So, F. (2015). High-Efficiency Solution-Processed Planar Perovskite Solar Cells with a Polymer Hole Transport Layer. *Advanced Energy Materials*, 5(6), p.n/a-n/a.

[80] Ramasamy, M., Mahapatra, S., Yoo, H., Kim, Y. and Cho, J. (2014). Soluble conducting polymer-functionalized graphene oxide for air-operable actuator fabrication. *J. Mater. Chem. A*, 2(13), pp.4788-4794.

[81] Baikie, T., Fang, Y., Kadro, J., Schreyer, M., Wei, F., Mhaisalkar, S., Graetzel, M. and White, T. (2013). Synthesis and crystal chemistry of the hybrid perovskite (CH3NH3)PbI3 for solid-state sensitised solar cell applications. *Journal of Materials Chemistry A*, 1(18), p.5628.

[82] Bi, C., Shao, Y., Yuan, Y., Xiao, Z., Wang, C., Gao, Y. and Huang, J. (2014). Understanding the formation and evolution of interdiffusion grown organolead halide perovskite thin films by thermal annealing. *J. Mater. Chem. A*, 2(43), pp.18508-18514.

[83] Kim, Y., Jeon, N., Noh, J., Yang, W., Seo, J., Yun, J., Ho-Baillie, A., Huang, S., Green, M., Seidel, J., Ahn, T. and Seok, S. (2015). Beneficial Effects of PbI2 Incorporated in Organo-Lead Halide Perovskite Solar Cells. *Advanced Energy Materials*, 6(4), p.1502104.

[84] Burschka, J., Pellet, N., Moon, S., Humphry-Baker, R., Gao, P., Nazeeruddin, M. and Grätzel, M. (2013). Sequential deposition as a route to high-performance perovskite-sensitized solar cells. *Nature*, 499(7458), pp.316-319.

[85] Bi, D., Tress, W., Dar, M., Gao, P., Luo, J., Renevier, C., Schenk, K., Abate, A., Giordano, F., Correa Baena, J., Decoppet, J., Zakeeruddin, S., Nazeeruddin, M., Gra tzel, M. and Hagfeldt, A. (2016). Efficient luminescent solar cells based on tailored mixed-cation perovskites. *Science Advances*, 2(1), pp.e1501170-e1501170.

[86] Zhao, D., Sexton, M., Park, H., Baure, G., Nino, J. and So, F. (2015). High-Efficiency Solution-Processed Planar Perovskite Solar Cells with a Polymer Hole Transport Layer. *Advanced Energy Materials*, 5(6)

[87] Jacobsson, T., Correa-Baena, J., Halvani Anaraki, E., Philippe, B., Stranks, S., Bouduban, M., Tress, W., Schenk, K., Teuscher, J., Moser, J., Rensmo, H. and Hagfeldt, A. (2016). Unreacted PbI2 as a Double-Edged Sword for Enhancing the Performance of Perovskite Solar Cells. *Journal of the American Chemical Society*, 138(32), pp.10331-10343.

[88] Chen, J., Shi, T., Li, X., Zhou, B., Cao, H. and Wang, Y. (2016). Origin of the high performance of perovskite solar cells with large grains. *Applied Physics Letters*, 108(5), p.053302.

[89] Serpetzoglou, E., Konidakis, I., Kakavelakis, G., Maksudov, T., Kymakis, E. and Stratakis, E. (2017). Improved Carrier Transport in Perovskite Solar Cells Probed by Femtosecond Transient Absorption Spectroscopy. *ACS Applied Materials & Interfaces*, 9(50), pp.43910-43919.

[90] Kakavelakis, G., Paradisanos, I., Paci, B., Generosi, A., Papachatzakis, M., Maksudov, T., Najafi, L., Del Rio Castillo, A., Kioseoglou, G., Stratakis, E., Bonaccorso, F. and Kymakis, E. (2018). Extending the Continuous Operating Lifetime of Perovskite Solar Cells with a Molybdenum Disulfide Hole Extraction Interlayer. *Advanced Energy Materials*, 8(12), p.1702287.